Realia et naturalia

DISSERTATIONES
CHIMICAE
UNIVERSITATIS
TARTUENSIS
150

PIRET PIKMA

Interfacial structure and adsorption of organic compounds at Cd(0001) and Sb(111) electrodes from ionic liquid and aqueous electrolytes: an in situ STM study

TARTU ÜLIKOOL · UNIVERSITAS TARTUENSIS · 1632

DISSERTATIONES CHIMICAE UNIVERSITATIS TARTUENSIS
150

DISSERTATIONES CHIMICAE UNIVERSITATIS TARTUENSIS
150

PIRET PIKMA

Interfacial structure and adsorption of organic compounds at Cd(0001) and Sb(111) electrodes from ionic liquid and aqueous electrolytes: an *in situ* STM study

UNIVERSITY OF TARTU
PRESS
1632

Institute of Chemistry, Faculty of Science and Technology, University of Tartu, Estonia

Dissertation is accepted for the commencement of the degree of Doctor of Philosophy in Chemistry on September 17th, 2015 by the Council of Institute of Chemistry, University of Tartu.

Supervisor: Prof. Enn Lust
Institute of Chemistry, University of Tartu, Estonia

Opponent: Prof. Pawel J. Kulesza
Department of Chemistry, University of Warsaw, Poland

Commencement: October 28th, 2015, at 10:00
14A Ravila Street, Tartu (Chemicum), auditorium 1021

ISSN 1406-0299
ISBN 978-9949-32-945-8 (print)
ISBN 978-9949-32-946-5 (pdf)

University of Tartu Press
www.tyk.ee

TABLE OF CONTENTS

1. LIST OF ORIGINAL PUBLICATIONS

I **P. Pikma**, V. Grozovski, H. Kasuk, E. Lust, *In situ* STM studies of electrochemically polished Cd(0001) electrode in aqueous electrolyte solutions, Surface Science, 628, 86−91 (2014).

II **P. Pikma**, H. Kasuk, O. Oll, V. Ivaništšev, T. Romann, V. Grozovski, K. Lust, E. Lust, Adsorption of 4,4′-bipyridine on the Cd(0001) single crystal electrode surface, Electrochimica Acta, 180, 965−976 (2015).

III **P. Pikma**, L. Siinor, S. Selberg, E. Lust, *In situ* STM studies of electrochemically polished Cd(0001) electrode in 1-ethyl-3-methylimidazolium tetrafluoroborate, ECS Transactions, 66 (27), 41−47 (2015).

IV **P. Pikma**, L. Siinor, O. Oll, E. Lust, Formation of 2,2′-bipyridine adlayers at Sb(111) | ionic liquid + 2,2′-bipyridine solution interface, Electrochemistry Communications, *accepted* (2015).

Author's contribution:

Paper I: Performed experimental surface measurements and data analysis. Collaborated in electrochemical data interpretation. Responsible for planning and writing the manuscript.

Paper II: Performed all experimental surface measurements and data analysis. Collaborated in electrochemical and theoretical data interpretation. Responsible for planning and writing the manuscript.

Paper III: Performed experimental surface measurements and data analysis. Collaborated in electrochemical data interpretation. Responsible for planning and writing the manuscript.

Paper IV: Performed all experimental surface measurements and data analysis. Collaborated in electrochemical and theoretical data interpretation. Responsible for planning and writing the manuscript.

2. ABBREVIATIONS AND SYMBOLS

2,2′-BP	2,2′-bipyridine
2D	two-dimensional
4,4′-BP	4,4′-bipyridine
A	adsorbance
ac	alternating current
AE	auxiliary electrode
ATR	attenuated total reflectance
c	concentration
C	differential capacitance
C_S	series capacitance
C_{tip}	tip capacitance
$C(0001)^C$	cleaved basal plane of highly orientated pyrolytic graphite
CV	cyclic voltammetry, cyclic voltammogram
d	distance
D	diffusion coefficient
e	energy of a particle
E	electrode potential
E_A	potential amplitude
E_{bias}	scanning tunneling microscopy tip bias potential
E_F	energy of Fermi level
E_{kin}	kinetic energy
E_{ox}	oxidation peak potential
E_{red}	reduction peak potential
E_{tip}	scanning tunneling microscopy tip potential
E_{WE}	working electrode potential
$E(t)$	potential at time t
EIS	electrochemical impedance spectroscopy
EC-STM	electrochemical scanning tunneling microscopy
$EMImBF_4$	1-ethyl-3-methylimidazolium tetrafluoroborate
f	frequency
F	Faraday constant
FFT	fast Fourier transform
FT	Fourier transform
FTIR	Fourier transform infrared spectroscopy
h	Planck constant
$\hbar$	reduced Planck constant
HOPG	highly oriented pyrolytic graphite
i	current density
i_{ox}	cyclic voltammetry oxidation peak current density
i_{red}	cyclic voltammetry reduction peak current density
I	electrode current
I_A	current amplitude
I_c	charging current

$I_{f,tip}$	faradaic current at the scanning tunneling microscope tip
$I_{f,WE}$	faradaic current at the working electrode
I_p	peak current
I_{WE}	working electrode current
I_{tip}	tip current
I_{tunnel}	tunneling current at the scanning tunneling microscope tip
$I(t)$	current at time t
IL	ionic liquid
IR	infrared
j	normal vibration
m	mass of a particle
n	number of electrons transferred
n_d	number of data points
pzc	potential of zero charge
q	normal coordinate describing the motion of atoms during a normal vibration
R	resistance
RE	reference electrode
RMS	root mean square roughness
RTIL	room temperature ionic liquid
S	surface area of the electrode
SEIRAS	surface enhanced infrared reflection absorption spectroscopy
SNIFTIRS	subtractively normalised interfacial Fourier transform infrared spectroscopy
STM	scanning tunneling microscopy
t	time
UHV	ultra high vacuum
V_{tip}	potentiostat controlling the potential of tip
V_{WE}	potentiostat controlling the potential of working electrode
WE	working electrode
z_i	height deviation of i-th point from the mean line
Z	complex notation of impedance
Z_0	magnitude of impedance
Z'	real part of impedance
Z''	imaginary part of impedance
$\delta c_{red}/\delta x$	concentration gradient of reduced species
λ_B	de Broglie wavelength
μ	molecular dipole moment
v	potential scan rate
$\rho_s(E_F)$	density of states at the Fermi edge
Φ	phase angle
ϕ	effective barrier height
ψ	wave function
ω	angular frequency

3. INTRODUCTION

Since the preparation of the first self-assembled monolayer of organic molecules adsorbed on top of an inorganic substrate, the field of organic-inorganic hybrid systems has rapidly developed theoretically as well as experimentally. Presently it is mainly driven by the highly requested advent of molecular electronics. However, properties achievable by combining the huge variety of organic materials with inorganic counterparts offers numerous applications beyond molecular electronics [1]. Some corresponding examples are surface passivation [2,3] corrosion protection [4–6], wetting or dewetting behaviour [7,8], lubrication [9–11], catalysis [12,13] and development of organic semiconductors for solar cells or organic light-emitting diodes [14]. Besides these mentioned technological aspects, behaviour of organic molecules on single crystal metal electrodes have become a model system for the study of structural transitions in adlayers and for the self-assembly of molecules on surfaces.

Room temperature ionic liquids (RTILs) are molten salts with poor coordination and weak interaction between the counterions which results in the liquid state of these ionic systems at room temperature [15,16]. Many RTILs have high stability under applied electrode potential, low vapour pressure, excellent thermal stability, *etc*. The RTIL | electrode interface attracts considerable attention, since it determines the characteristics of various electrical power sources, including supercapacitors and novel batteries [17–19].

Scanning tunneling microscopy (STM) is an extremely useful method for detailed analysis of the surface structure of solid materials, including super-capacitors, fuel cells, Li-ion and Na-ion batteries, *etc*. STM method allows obtaining the high-resolution images of different conductive surfaces and adsorbed adlayers. It enables to visualise the electrode surface structure *in situ* at the atomic/molecular resolution level, to determine the potential dependence of the deposited adlayers structure and to establish also the surface atomic structure of many single crystal metal electrodes under *in operando* conditions [20–22].

The structure and stability of an adsorbed monolayer strongly depends on the crystallographic structure of the single crystal plane studied, influencing the adsorbate-adsorbent interaction, as well as the adsorbate-adsorbate, adsorbate-electrolyte ions, adsorbate-solvent and solvent-solvent lateral Gibbs interaction energies [23–29]. Therefore in recent years the electrolyte | electrode interface characteristics have attracted considerable attention in fundamental and applied electrochemical studies. However, most of these studies investigate the electro-chemical behaviour of Pt, Au and C electrodes. In addition, the interfacial characteristics for the electrolyte | metal electrode interface with high hydrogen overvoltage (like cadmium, antimony, *etc.*) interface should also be investigated to gain better understanding of the fundamental parameters of the metal electrode | electrolyte interface.

Cadmium (Cd) and antimony (Sb) single crystals as very good model electrodes with the stable surface structure in a wide potential region have been studied at the University of Tartu since the 70's. An extensive database has been collected, containing a lot of information about the influence of the chemical nature and crystallographic structure of electrodes as well as the structure of the adsorbing anions or neutral organic compounds on the adsorption parameters [30–40].

According to our knowledge, there are no data describing the Cd(0001) single crystal electrode | electrolyte interface structure at the atomic level resolution. Therefore one aim of this work was to study the surface structure of Cd(0001) single crystal electrode in various electrolytes (including RTIL) and to develop conditions needed to obtain the atomic resolution *in situ* STM data within the wide polarisation region of the Cd(0001) electrode, since only proper correlation of electrochemical and STM measurements allows a reasonable interpretation of observed changes on an electrode surface.

During the experimental part of the present work, it became obvious, that in addition to the atomic resolution of Cd electrode surface structure, achieved *in situ* in aqueous electrolyte [I] and in ionic liquid [III], it is possible to visualise the adsorbed molecules of 4,4′-bipyridine (4,4′-BP) on the electrode surface under different polarisation conditions [II]. Similar experiments have been conducted on the Hg, Au and Bi single crystal electrodes and adsorption of 2,2′-bipyridine (2,2′-BP), 4,4′-BP and camphor have been demonstrated [23,27–29,41–46].

Another aim of this work was to study the interfacial structure between Sb(111) and an ionic liquid [IV]. During the measurements the atomic resolution was achieved and compared to previous results in surface inactive electrolyte [47]. These data were used to investigate the adsorption process of 2,2′-BP from RTIL [IV].

In this work in addition to the *in situ* STM method, cyclic voltammetry (CV), electrochemical impedance spectroscopy (EIS) and infrared methods were also applied for analysis of the surface structure of the single crystal electrode | electrolyte interface and to study the 2,2′-BP and 4,4′-BP adsorption at the single crystal electrodes.

4. LITERATURE OVERVIEW

4.1. The properties of Cd

Cadmium is a group II-B element with outer electron configuration $4d^{10}5s^2$. Cadmium is regarded as non-transition element, since it forms no compound in which the *d* shell is other than full [48].

Cadmium finds a lot of applications, such as a barrier in nuclear reactors to control neutrons owing to its high potential to absorb low energy neutrons; rechargeable Ni–Cd batteries; Cd or Cd alloy (*i.e.* Ag-In-Cd) rods are used for controlling the fission process in nuclear reactors; red/yellow pigments owing to their features like insolubility in inorganic solvents, water and stable behaviour against ultraviolet light and heat. Cd is also used as a precursor material for fabrication of many important cadmium based semiconductors such as cadmium sulphide (CdS), cadmium selenide (CdSe), cadmium oxide (CdO) and cadmium zinc telluride (CdZnTe), *etc*. [49].

Cadmium forms a protective oxide film that reduces Cd corrosion/oxidation rate in atmospheric conditions. Cd exhibits low corrosion rates in solutions with pH from 5 to 10. However, in more acidic and alkaline environments, corrosion rates of Cd increase dramatically [50]. From the Pourbaix diagram it can be seen that at pH $\leq$ 5 and at electrode potential $E \geq -0.80$ V (*vs.* Ag | AgCl sat. KCl) the following electrochemical dissolution reaction takes place [51]:

$$Cd = Cd^{2+} + 2e^{-}. \quad (1)$$

The crystal structure of cadmium is hexagonal close-packed with cell parameters $a = 2.9793$ Å and $c = 5.6181$ Å (Fig. 1) [52,53].

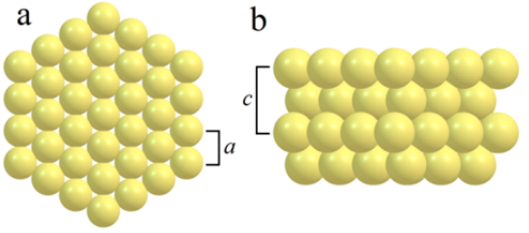

Figure 1. Crystallographic structure of cadmium.

The shape of the cyclic voltammograms (CVs) and EIS spectra for Cd(*hklf*) planes do not depend noticeably on the electrode potential scan direction, from more negative potentials towards less negative potentials or vice versa, as well as on the potential scan rate (ν) within the region of ideal polarisability of the Cd(*hklf*) electrode and probably there is no quick Cd(*hklf*) surface

reconstruction [32,34–36,54]. Thus, based on the CV and EIS data the surface reconstruction phenomena do not take place on Cd(0001) single crystal plane.

4.2. The properties of Sb

Antimony is an element from group V-A with outer electron configuration $5s^2 5p^3$ [55].

The crystal structure of antimony is rhombohedral with cell parameters a = 4.3084 Å and c = 11.27 Å (Fig. 2) [56,57].

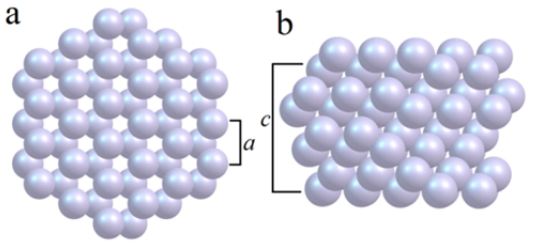

Figure 2. Crystallographic structure of antimony.

The double layered crystal structure of Sb, where each atom has three close neighbours from the same layer (s^2p^3-electronic configuration; the distance between atoms is 2.91 Å) and three farther neighbours from the second neighbouring layer bonds with the aim of hybrid sp^3d^1 orbital (the distance between atoms in neighbouring layers is 3.35 Å) [56].

The metallic properties of the fifth group elements depend on the bonding between neighbouring layers [55]. The presence of the covalent bonds between the atoms in the Sb lattice probably fixes the position of the surface atoms more rigidly than in the case of typical *sd*-metals (Au, Cu, Pt, Pd) [37,58–62].

The unique electronic properties of Sb, its small Fermi energy combined with highly anisotropic electron and hole masses and carrier concentrations several orders of magnitude lower than in noble metals makes Sb a prime candidate for novel thermoelectric converters. Devices based on nano-scale particles/structures of Sb and Bi (or their alloys) are thereof among those with the highest conversion efficiency [63].

According to the previous CV, EIS, chrono-coulonometry and *in situ* STM studies [30–37,39,47,32,64], there is no quick surface reconstruction of Sb(*hkl*) within the region of ideal polarisability of Sb(111) electrode.

4.3. Ionic liquids

Ionic liquids (ILs) are a class of purely ionic, salt-like materials that are liquid at unusually low temperatures. The official definition of ILs uses the boiling point of water as a point of reference: “Ionic liquids are ionic compounds which are liquid below 100 °C”. In particular, salts that are liquid at room temperature are called room temperature ionic liquids. RTILs, also known as organic liquids, molten or fused salts, are a class of non-molecular ionic solvents with low melting points. The widely accepted definition of a RTIL is: “Any salt that has a melting point lower than ambient temperature” [65].

As a class, ionic liquids have been defined to have melting points below 100 °C and most of them are liquid at room temperature. Both cations and anions contribute to the low meting points of ionic liquids. The increase in anion and cation size generally leads to a decrease in melting point. Cation symmetry also makes an important impact – increased asymmetric substitution results in a melting point reduction [66].

ILs have reasonable ionic conductivities at room temperatures compared with organic solvents and organic solvent based electrolyte systems (up to 30 mS cm^{-1}). At elevated temperatures, *e.g.* 200 °C, a conductivity of 100 mS cm^{-1} can be achieved for some systems. However, at room temperature their conductivities are usually lower than for concentrated aqueous electrolytes. The large constituent ions of ILs reduce the ion mobility which, in turn, leads to lower conductivities. Furthermore, for some RTILs ion aggregation leads to reduced conductivity. The conductivity of ILs is inversely linked to their viscosity. Hence, ILs of higher viscosity exhibit lower conductivity. Increasing the temperature decreases viscosity and increases conductivity [66].

Generally, ILs are more viscous than common molecular solvents and their viscosities are ranging from 10 mPa s to about 500 mPa s at room temperature. The viscosity of ILs is determined by the van der Waals forces, hydrogen bonding and also by electrostatic forces. Alkyl chain lengthening in the cation leads to an increase in viscosity, since stronger van der Waals forces between cations increase the energy required for molecular motion. Also, the ability of anions to form hydrogen bonds has a pronounced effect on viscosity [66].

ILs have mostly higher density than water with values ranging from 1.3 g cm^{-3} for typical ILs to 2.3 g cm^{-3} for bulky ILs. The density of ILs strongly depends on the length of the alkyl chain in the cation, on the symmetry of ions and on the strength of interaction forces between the cation and the anion. Generally ILs with aromatic head ring have greater densities than ILs based on pyrrolidinium or piperidinium rings. ILs that have more symmetric cations have higher density. Also ILs with polar functional group(s) are denser than ILs with alkyl chains [65].

ILs can be thermally stable up to temperatures of 450 °C. The strength of carbon-hydrogen bonds limits their thermal stability. Nonetheless, majority of ILs withstand such high temperatures only for a short time. Long exposure to high temperatures leads to decomposition [66].

Most of the ILs have extremely low vapour pressures, which enables water removal by heating under vacuum. Therefore it is relatively easy to achieve water content under 1 ppm in numerous ionic liquids [66].

The region of ideal polarisability of an electrolyte is defined as the electrochemical potential range over which the electrolyte is neither reduced nor oxidised at an electrode surface. ILs have significantly wider region of ideal polarisability than aqueous electrolytes [16].

Due to RTILs high stability under applied electrode potential, low vapour pressure, excellent thermal stability, high ionic conductivity, non-flammability and tuneable counterpart ions the RTIL | electrode interface attracts considerable attention determining the characteristics of various electrical power sources, including batteries, fuel cells, *etc*. [17–19]. In particular, the wide region of ideal polarisability and dual usability as solvents and electrolytes opened interesting possibilities in the field of fundamental and applied electrochemical studies. For instance, RTILs have been already used as electrolytes in supercapacitors, in electrodeposition of metals and alloys, in electrocatalysis and in energy storage devices, and for optimising the rate and even mechanism of heterogeneous reactions [16].

Air-stable and water-stable ILs are increasingly employed to progressively replace organic solvents in a variety of chemical processes due to their non-volatile behaviour, non-flammability, and in some cases, stability at temperatures over 400 °C [67].

RTILs are also considered as possible electrolytes for gas sensing applications, since their favourable properties (low-volatility and high thermal stability) mean that the sensor does not dry out, and provides the possibility for gas sensing at high temperatures [68].

In 1992, Wilkes and Zaworotko reported the first air and moisture stable ionic liquids based on 1-ethyl-3-methylimidazolium cation with either tetrafluoroborate or hexafluorophosphate anion [15]. Although the melting point of 1-ethyl-3-methylimidazolium tetrafluoroborate ($EMImBF_4$) (15 °C) is too high for many practical applications, it is a widely used RTIL for analysing the influence of the chemical nature of different metal or carbon electrodes on the RTIL | metal (including single crystals) or carbon electrode interface parameters [69–72].

4.4. Scanning tunneling microscopy (STM)

The development of reliable instruments for characterisation of microstructure, physical and chemical properties of materials has improved the understanding of processes taking place at different solid | gas and solid liquid interfaces at the micrometric, nanometric and angstrom- (atomic-) scale. Although it is possible to gain information about the surface structure by scanning electron microscopy, high-resolution examination of local electronic structure, influence

of electrode potential on the surface structure and chemical functionality are much more challenging.

The development of scanning tunneling microscopy (STM) by Binning and Rohrer in 1981 [73] made it possible to study local electronic properties. The technique soon became an indispensable method in surface science with atomic resolution in ultra-high vacuum (UHV) and earned its authors the Nobel Prize in physics (1986). The first real-time surface topography image with an instrument operated in air at ambient pressure within a wide resolution range has been achieved at Au and Pt electrode surfaces by Gomez *et al.* [74–76]. In 1986 the STM technique was further developed by Sonnenfeld and Hansma to operate in electrolyte solutions [77].

While the first electrolytic STM applications were performed with a conventional STM instrumentation adapted for operating in an electrolyte, in 1988 the potentiostatic STM method was introduced [78–80].

Electrochemical STM, *in situ* STM (also termed EC-STM), is a powerful technique for studying the structural effects of electrochemical processes taking place at the metal electrode | electrolyte interfaces. Thus, *in situ* STM enables the localisation of electrochemical reactivity if it is accompanied by changes in sample topography, *e.g.* can be used to study underpotential deposition, structures of adsorbed species and electrochemical dissolution reactions of electrode.

Nowadays the *in situ* STM can operate at ambient conditions with four-electrode configuration where the electrochemical potential of the tip and the substrate can be independently controlled with respect to a common reference electrode.

4.4.1. Main aspects of STM

In STM, a weak potential difference is applied between the studied sample (working electrode) and a conductive tip, which ideally has an atomically sharp end. These two conducting electrodes (tip and sample) are separated by some sort of isolator (air or liquid), which forms a barrier for the electrons inside the electrodes. The flow of tunneling current between tip and sample is possible as long as the tip-sample distance is smaller than few nanometres. Electron tunneling originates from the overlap of wave functions between the particles at the tip and the surface atoms of the working electrode. According to quantum mechanics, a wave-like particle with energy e can penetrate a barrier with effective barrier height $\phi > e$. Within the classical forbidden region, the wave function ψ decays exponentially

$$\psi(z) = \psi(0) exp\left[-\frac{\sqrt{2m(\phi - e)}z}{\hbar}\right], \quad (2)$$

where m is the mass of the particle and $\hbar$ = 1.05×10^{-34} J s. It describes the penetration of an electron through the barrier into vacuum. The probability density of observing an electron near distance z in vacuum or electrolyte is proportional to $|\psi(0)|^2 e^{-2kz}$, which has a nonzero value in the barrier region. Therefore there is a finite probability that a particle penetrates the barrier. Another conclusion that can be made from Equation 2 is that the tunneling is bidirectional as $\psi(z) \neq \psi(-z)$. In UHV STM the barrier is given by the vacuum gap between sample and tip. Thus, the tunneling current, I_{tunnel}, can be estimated by considering the density of states of the sample, $\rho_s(E_F)$, at the Fermi edge:

$$I_{tunnel} \propto E_{bias}\rho_s(E_F)exp\left[-2\frac{\sqrt{2m(\phi-E)}z}{\hbar}\right] \propto V\rho_s(E_F)e^{-1.025\sqrt{\phi}z}, \qquad (3)$$

where E_{bias} is the bias potential between the tip and the working electrode, and the barrier height ϕ is expressed in electron volts (eV) and distance z in angstroms (Å). Typical tunneling currents fall in the order of nanoampere (nA), which requires high amplifications that limit the bandwidth to a few kilohertz (kHz) [81,82].

The tunneling barrier can be formed by a vacuum, gas, or an electrolyte solution. However, in the latter case, the STM tip has to be considered as an additional electrode, as shown in Fig. 3. This results in faradaic currents at the tip ($I_{f,tip}$) due to electrochemical reactions at the tip surface and as a contribution to the tip capacitance, C_{tip}, caused by the electrical double layer of the tip, which both interfere with the STM measurement.

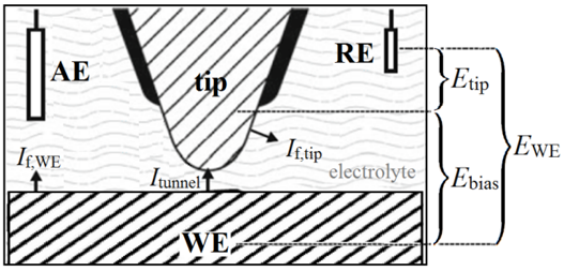

Figure 3. Schematic illustration of the electric configuration of *in situ* STM, showing the tunneling tip and working (WE), reference (RE), and auxiliary (AE) electrode, where E_{WE}, E_{tip}, E_{bias} are the potentials of WE and tip and their difference, respectively, *vs.* RE; I_{tunnel} is the tunneling current; I_{WE}, I_{tip} are the currents at WE and tip, respectively; and $I_{f,WE}$, $I_{f,tip}$ are the faradaic currents at WE and tip, respectively. The coating of the tip is indicated in black [22].

The electrochemical currents at the tip have to be suppressed, since only the sum of tunneling and faradaic currents (I_{tunnel} + $I_{f,tip}$) can be measured. Stable

STM measurement is only possible if the tunneling current is considerably larger than the faradaic current at the tip ($I_{tunnel} >> I_{f,tip}$).

It is also important to minimise C_{tip} for an optimised signal-to-noise ratio, because the noise in the high-gain current-potential converter used to measure the tip current increases with increasing input impedance (total resistance). In particular for studies at low tunneling current or high recording speeds low C_{tip} values are extremely important.

Both $I_{f,tip}$ and C_{tip} can be remarkably reduced by coating the tip with an electric insulator, leaving only a μm-sized area at the tip apex uncovered. The coating material should exhibit high chemical stability in the electrolyte solution, to avoid contamination of the sample surface and electrolyte. Usually Apiezon^{TM} wax, polymer coatings, or electrophoretic paints are used, enabling routine preparation of tips, where $I_{f,tip}$ is reduced below 10 pA and C_{tip} to a few pF [22].

$I_{f,tip}$ can be additionally minimised by keeping the tip potential in the so-called double layer regime. This also inhibits electrochemical reactions (oxidation, dissolution, deposition) at the tip that cause structural changes in the tip shape. It requires that not only the potential of the working electrode, E_{WE}, but also the tip potential, E_{tip}, is controlled with respect to a reference electrode [22]. Therefore *in situ* STM experiments require the use of a bipotentiostat in order to separately control the electrochemical potential of the tip and the potential of the working electrode *vs*. reference electrode (Fig. 4) with a design adapted to the rather different current ranges of tip (pA to nA) and sample (typically ≥ μA).This configuration is different from experiments carried out in UHV in which only the bias between the electrodes needs to be specified [20].

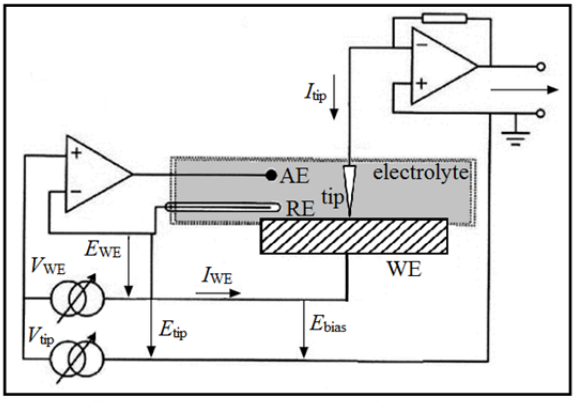

Figure 4. Schematics of *in situ* STM system with a bipotentiostat, where WE is the working electrode; RE is the reference electrode; AE is the auxiliary electrode; E_{WE}, E_{tip}, E_{bias} are the potentials of working electrode and tip and their difference, respectively, *vs.* RE; I_{WE}, I_{tip} are the currents at WE and tip, respectively; V_{WE}, V_{tip} are the potentiostats controlling the potential of the working electrode and the tip, respectively [20].

During *in situ* electrochemical studies when the sample potential, E_{WE}, is changed, the tip bias, E_{bias}, or the tip potential, E_{tip}, can be kept constant. The first mode ensures constant tunneling conditions but may require limiting the accessible range of E_{WE} to maintain E_{tip} in the double-layer regime of the tip. In the second mode, the electrochemical conditions at the tip, and consequently $I_{f,tip}$ is independent of E_{WE}. The variation of E_{bias} in this mode usually does not have a strong effect on the STM imaging of/at metal substrates, where the dependence on E_{bias} is weak. However, for *in situ* STM studies of semiconductors, where both tunneling and electrochemical conditions have strong impact on the measurement, it is extremely difficult to establish potentials that allow stable imaging [22].

The impact of solvated ions to the tunneling process has had little attention since it is highly improbable that these species exist in the junction during atomically resolved imaging. However, ions that are specifically adsorbed on the working electrode or on the tip will change the local density of states and the surface dipole, thereby altering the distribution of the electrostatic potential within the gap in a manner analogous to the vacuum junctions [83,84]. The adsorbate still contributes to the local density of states upon adsorption, even though the atomic resonance of an adsorbate lies far above the Fermi level, due to the significant broadening of the resonance [83]. When the orbital contributes to the image formation, it extends significantly out from the surface than the bare substrate wave functions [83,85,86]. It has been found that in the case of simple anions that have adsorbed on the metal surface, the extension of orbitals in space has more impact to image formation than the energy of the adsorbate orbitals. However, it has been shown that the image formation in such systems is highly sensitive to the tunneling conductance [85,86].

If a bias potential is applied to the sample, an electron tunneling current flows between the two phases. Depending on the bias polarity, electron transfer can either be established from occupied states of the sample into unoccupied states of the tip (positive bias potential) or *vice versa* (negative bias potential) [81]. The tunneling current between the conductive sample and the tip is measured as a function of the distance travelled in the x and y directions. The direction of the electron flow depends on the sign of the bias applied to the sample.

Measurement of the current is sensitive of the order of magnitude necessary to resolve atomic or molecular corrugations on the surface of the sample. If electrons are tunneling from a sharp metallic tip to a flat metallic electrode or similar substrate, two different situations can be observed. In the case of large tip-substrate separation, much greater than the de Broglie wavelength,

$$\lambda_B = \frac{h}{(2meE)^{1/2}} = \frac{1.2}{E^{1/2}}, \quad (4)$$

in nm, where h is the Planck constant, and E is the applied potential (V), electrons can only penetrate the gap when high electrical potential is applied,

which is the case in field emission. On the other hand, when the distance between the tip and working electrode is approximately λ_B, as is the case in STM, electrons can tunnel directly across the gap when a small bias potential is applied. This allows one to obtain information about the surface at the atomic resolution level. The interaction between the probe tip and the sample varies exponentially with the distance between the sample and the most extreme tip on the probe. Thus, in the case of STM, the atom at the tip apex allows the tunneling current to pass through [87].

The high spatial resolution of the STM is due to the exponential dependence of the tunneling current on the tip-sample distance. The resolution in the direction normal to the surface achieves fractions of angstrom. The lateral resolution depends on the quality of the tip and is determined primarily not by the macroscopic curvature radius of the tip apex, but by its atomic structure. If the tip has been correctly prepared, there is either a single projecting atom at the apex, or a small cluster of atoms, with the size much smaller than the mean curvature radius of the tip apex. In fact, the tunneling current flows between atoms placed at the sample surface and atoms of the tip. An atom, protruding from the tip, approaches the surface to a distance comparable to the crystal lattice spacing. In this case the current flows between the sample surface and the projecting atom at the apex of the tip [88]. Using well-prepared tips it is possible to achieve a spatial resolution down to atomic scale, as demonstrated by many research groups using samples of various materials.

As mentioned, the STM topographic image of a surface can be formed in two ways. In the constant current mode (Fig. 5a) a feedback mechanism permits to tune the vertical position of the tip whilst keeping the constant tunneling current, *i.e.* an STM image displays the variations of the tip vertical position while horizontally scanning the sample. During this the potential signal applied to the *z*-electrode of a piezoelement in the feedback circuit (the tip-sample distance is kept constant with high accuracy) is recorded as a $z = f(x,y)$ function, and is later plotted using the computer graphics.

During the investigation of atomically flat surfaces it is often more effective to measure the STM image in the constant height mode ($z = const$) (Fig. 5b). In this case the tip moves above the surface at a constant height of several angstroms and the changes in the tunneling current are recorded as STM image. Scanning may be done either with the feedback system switched off (no topographic information is recorded), or at a speed exceeding the feedback reaction speed (only smooth changes of the surface topography are recorded). Applying mentioned method very high scanning rates can be applied and STM images are created very quickly, allowing to observe the changes occurring on the surface practically in real time [88].

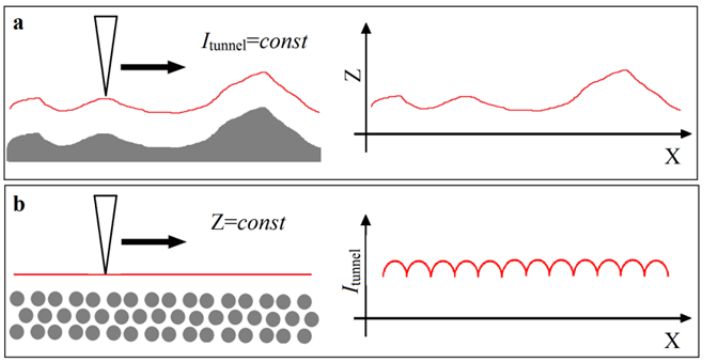

Figure 5. Schematic illustration of the formation of STM images in the constant current mode (a) and in the constant height mode (b), where I_{tunnel} is the tunneling current and Z is the position of the tip in the z-direction [88].

In order to carry out atomically resolved *in situ* STM studies at solid electrode surfaces, the surface has to be very flat with well-defined crystallographic structure and routinely restorable to its original conditions [58]. Many methods have been introduced over the years to achieve atomically flat surface structure. Flame annealing in a hydrogen-oxygen flame has proven to be particularly convenient in the case of the Au and Pt single crystal surfaces [59–61,89–96]. Electrochemical and chemical polishing is a widely used method to prepare the surfaces of various metal electrodes, *e.g.* Bi [23,45,97–99], Cd [100–104] and Sb [47]. Another method for preparing well-defined surfaces is electrochemical capillary growth techniques for deposition of the single crystals which can be used to grow single crystals, *e.g.* Ag single crystals [105,106]. Atomic layer deposition from the gas phase, electron-beam evaporation as well as different sputtering methods are also used for producing surfaces with reasonable surface roughness and exact orientation [69,105,107]. However, during systematic studies it was found that the surface mesoscopic structure noticeably depends on the specific preparation method used and different effects, like step bunching, can occur [25,26,55,58,59,90–93,96,105–110].

Additionally the influence of the applied electrode potential during an *in situ* STM experiment has been thoroughly investigated. The dependence of the surface structure of Au(*hkl*), Pt(*hkl*) and Ag(*hkl*) and other face centred cubic metals on the applied electrode potential has been discussed in many papers [25,26,59–61,89,91–93,110]. It was found that the surface structure of Au(*hkl*) electrodes is highly dependent of the surface charge density. Therefore, it depends on the difference of electrode potential applied with respect to the potential of zero charge (pzc). Also it has been noted that the electrochemical work function values essentially depend on the electrode preparation methods used, as well as on the other experimental conditions applied [37,61].

4.5. Infrared spectroscopy

Over the last two decades, *in situ* infrared (IR) spectroelectrochemistry has become an increasingly applied powerful analytical tool in electrochemistry, and has developed strongly in terms of the diversity of electrochemical systems that have been studied. This transition may be associated with the availability of relatively inexpensive, research grade Fourier transform infrared (FTIR) spectrometers. In contrast to the early 80's, the detection of organic monolayers is now commonplace and there is other exciting work in fields as diverse as organometallic spectroelectrochemistry. In-depth studies of the double layer, time-resolved studies, (photo-)electrocatalysis as a function of temperature and the semiconductor | electrolyte interface have been conducted [111].

IR spectroscopy is an analytical technique for identification of chemical compounds. It is based on the fact that different chemical functional groups absorb infrared light at different wavelengths dependent upon the nature of the particular chemical functional groups present in the adsorbate. The method is fast, sensitive, relatively easy to handle and provides many different sampling techniques for gases, liquids and solids. Important aspects are the convenient qualitative and quantitative evaluation of the spectra [111–113].

IR instruments can be operated in either the transmission or reflectance mode. In the past, analyses were often limited by the thickness of the samples, by the shape of the sample, by the bulk quantity of the sample and by the quality of the surface of the sample. These restrictions have been mostly overcome with adapters that change the presentation of the samples to the IR beam. Attenuated total reflectance (ATR) and diffuse reflection accessories allow the analysis of the surface of the coatings and allow comparison of the bulk properties with the surface properties of a material [112,113].

The IR region comprises fundamental vibrations of bound atoms. Whenever such bound atoms vibrate, they absorb infrared radiation, *i.e.* they exhibit IR absorption bands. The condition for a normal vibration j to be IR active is a change in molecular dipole moment μ during vibration:

$$\mu_j = \mu_0 + \left(\frac{\delta\mu}{\delta q_j}\right) q_j + \frac{1}{2}\left(\frac{\delta^2\mu}{\delta q_j^2}\right) q_j^2 + \cdots , \qquad (5)$$

where q is the normal coordinate describing the motion of atoms during a normal vibration. With respect to the direction of the vibrational movement we may distinguish between stretching vibrations (changes of bond lengths) and deformation vibrations (changes of bond angles). Deformation vibrations may be subdivided into bending modes, twisting or torsion modes, wagging modes and rocking modes. Further subdivision refers to the symmetry of the vibration (*e.g.* symmetric or antisymmetric, in-plane or out-of-plane) [112].

A Fourier Transform (FT) is a mathematical conversion that allows the split of the entire infrared light spectrum simultaneously, then converting the scanning results mathematically into a wavelength *vs.* transmittance spectra.

Combined together these two functions provide FTIR as an instrument that can be used in the identification and characterisation of organic compounds. The relative simplicity of the resulting FTIR analytical methods allows it to be widely used for the analysis of a wide range of different materials. It is often used in the packaging industry to analyse monomeric materials for purity, and to identify polymers (polyethylene, polyester, nylon, *etc*.) and their compositions [113].

The non-electrochemical spectroscopy surface enhanced infrared reflection absorption effect was first reported by Hartstein and co-workers in 1980 [114]. Osawa *et al.* pioneered the application of this technique for *in situ* electro-chemical IR studies on metal thin films [115]. Surface enhanced infrared reflection absorption spectroscopy (SEIRAS) spectra show marked enhancement of the infrared absorptions of adsorbed species, up to 40 times of that expected on a smooth, bulk metal electrode. A thin metal overlayer excites surface plasmon polaritons in the metal film, the strong electromagnetic fields associated with this excitation provide a sensitive probe of the metal film | electrolyte interface, with tenfold enhancement in sensitivity being claimed over the more conventional subtractively normalised interfacial Fourier transform infrared spectroscopy (SNIFTIRS) method [111].

The mechanism has two distinct parts that complement each other to give the observable large enhancement effect. The surface plasmons of the metal island films are excited by electromagnetic mechanism. If the molecules reorient in a way that their dipole moments are in line with the electric field on the islands then the molecules will absorb more energy from the source radiation.

The other part consists of chemical interactions. The only well-known and understood effect is chemisorption. The chemisorbed molecules can reorient when the electric field is induced on the surface of the metal, resulting in a much higher enhancement factor. In the case of physisoption this effect does not occur. However, other chemical interactions seem to be occurring as well, since the calculated enhancement effect is still lower by a factor.

The application of SEIRAS to electrochemistry can be very wide. One example of this is the use of SEIRAS to gain information about the mechanism of irreversible electrochemical reactions. However, SEIRAS can also be applied to study the structure of the electric double layer at the electrochemical interface. This is of great importance because it helps to understand electrocatalytic reactions. Furthermore, it is possible to monitor reversible reactions by microsecond time resolution.

Both the electrolyte and the metal layer are damping the evanescent wave by absorbing energy from it. Hence, it is crucial to ensure that the metal working electrode layer, whilst being thick enough to ensure metallic conductivity, is not too thick that the evanescent wave is not sufficiently damped and it cannot sample the electrode | electrolyte interface [111].

The application of ATR-SEIRAS (Fig. 6) experiments at solid/liquid interfaces with well-defined metal films deposited on highly refractive IR-transparent prisms has several advantages, in comparison to SNIFTIRS

studies employing the so-called thin electrolyte film configuration (1 μm to 5 μm) between the optical window and the working electrode: 1) high and specific surface sensitivity with an enhancement up to *ca*. 40 times stronger as in SNIFTIRS; 2) dominant first layer effect (dense layer region) with a short decay length of the enhanced field of 3 nm to 4 nm (diffuse layer region) towards the bulk electrolyte; 3) signals from the interface and the solution background are of comparable magnitude and can be separated by applying the potential difference tactics; 4) no severe limitations due to mass transport and potential perturbations [44].

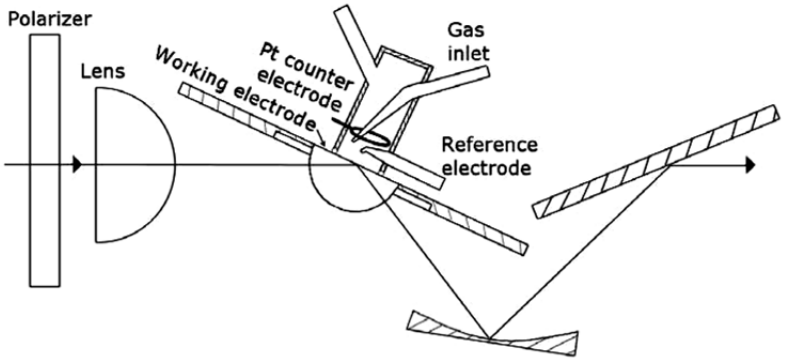

Figure 6. Constructed variable angle (55−75 deg) SEIRAS spectroelectrochemical cell with corresponding IR beam path [116].

The SEIRAS spectra are governed by both concentration induced changes as well as by the action of surface selection rule. Changes of adsorbate concentration at the interface result in all the vibrational modes of a given species to be in the same direction. The surface selection rule for IR spectroscopy states that only interfacial changes that produce a net positive dynamic dipole moment perpendicular to the interface are enhanced by the plasmonic properties of the electrode material, while dynamic dipole changes parallel to surface (perpendicular to the electric field caused by the electronic plasma oscillations) are not enhanced [70,116,117]. This means that, differently from the concentration induced changes, adsorbed species can have both positive and negative going bands in the SEIRAS spectra, dependent on the orientational changes of the adsorbed species initiated by changing the electrode potential.

SEIRAS method has been mainly used for analysing coinage metals and platinum surfaces, but it was shown by Romann *et al.* that this method could be used also for analysis of adsorbed layers at other metals like Bi [45,116].

4.6. Cyclic voltammetry (CV)

Cyclic voltammetry is the most widely used and often the first experiment performed for acquiring qualitative and quantitaive information about the electrochemical reactions and charging of electrical double layer.

In CV method, the electrode potential, E, is changed cyclically with a constant scan rate, $\nu = dE/dt$, between two potential extremes (*i.e.* the applied potential varies in saw tooth like fashion (Fig. 7a)), and the corresponding current is recorded. The resulting current *vs*. potential plot, known as the cyclic voltammogram (Fig. 7b), gives a survey over the processes occurring within the potential range studied [118–120].

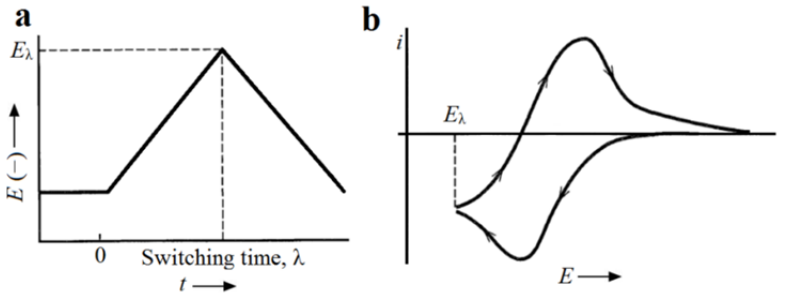

Figure 7. Cyclic potential sweep (a) and resulting cyclic voltammogram (b), where i is the current density, E is the electrode potential, t is the time and E_λ is the electrode potential at switching time λ [118].

For a simple redox reaction, it is possible to express the temporal development of the current density, i, through the electrode:

$$i = nFD\left(\frac{\partial c_{red}}{\partial x}\right)_{x=0}, \tag{6}$$

where n is the number of electrons transferred, F is the Faraday constant, D is the diffusion coefficient, $\delta c_{red}/\delta x$ is the reduced species concentration gradient. For a reversible one electron transfer process ($n = 1$), when the diffusion coefficients for oxidised and reduced form are equal, the difference between oxidation and reduction current density peak potentials should be 58 mV [118,120].

Usually the electrode potential is scanned linearly towards a more negative potential and back towards the starting potential. The forward scan produces a current peak for any species that can be reduced within the range of the potential scan. The current density absolute value, $|i|$, will increase as the potential reaches the reduction potential of the species, but then falls off as the concentration of the species is depleted close to the electrode surface. As the

applied potential is reversed, it will reach a potential that will oxidise the product formed during the reduction reaction, and produce a current of reverse polarity from the forward scan. This oxidation peak will usually have a similar shape to the reduction peak. The peak current, I_p, is described by the Randles-Sevcik equation:

$$I_p = (2.69 \times 10^5)\, n^{3/2}\, Sc\, D^{1/2}\, v^{1/2}, \quad (7)$$

where S is the area of the electrode and c is the species concentration, [118,121].

The electrochemical reactions at the surface can be divided into two major groups: adsorption controlled processes and diffusion controlled processes. In case of the adsorption step limited process the current peak height is proportional to the applied sweep rate and the charge circulated during the sweeps provides information on the surface coverage of the adsorbed species. However, for diffusion step rate controlled process, the peak current height is proportional to the square root of the potential sweep rate [118,121].

The exact shape and quantitative features in CVs depend on various parameters, *e.g.* the adsorbed species, the adsorption isotherm followed, the surface concentration of the redox species, or on the presence or absence of intermolecular forces between the adsorbed molecules [120].

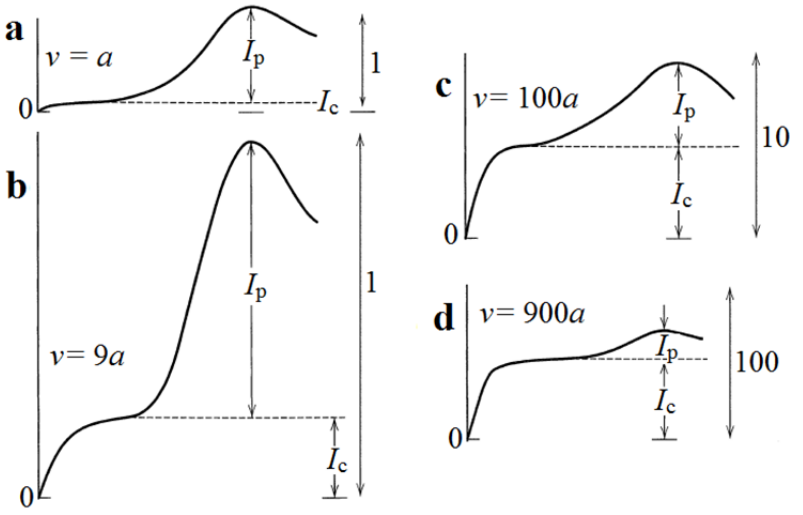

Figure 8. Effect of double-layer charging at different potential scan rates (v) on a linear potential sweep voltammogram. Curves are plotted with the assumption that differential capacitance is independent of potential. The magnitudes of the charging current, I_c, and the peak current, I_p, are shown with respective current scales [118].

Since the potential is continuously changing in a potential sweep experiment, a charging current, $|I_c|$, always flows:

$$|I_c| = SCv, \tag{8}$$

where C is the differential capacitance. Thus the faradaic current must always be measured from a baseline of charging current (Fig. 8) [118].

4.7. Electrochemical impedance spectroscopy (EIS)

Electrochemical impedance spectroscopy (EIS) methods were initially applied to determine the double-layer capacitance. Nowadays the EIS methods are regularly used to characterise electrode processes and complex interfaces. EIS studies the system response to the application of a periodic small sinusoidal ac potential signal by measuring the current through the electrochemical cell. These measurements are carried out at different ac frequencies. Analysis of the system response contains information about the interface properties, its structure and reactions taking place at the interface [122].

During the experiments usually sinusoidal perturbation is applied to the electrochemical system:

$$E(t) = E_A \sin \omega t, \tag{9}$$

where $E(t)$ is the potential at time t, E_0 is the potential amplitude, ω is the angular frequency with a relationship to frequency (f): $\omega = 2\pi f$. The current response $I(t)$ will be a sinusoid at the same frequency but shifted in phase:

$$I(t) = I_A \sin(\omega t + \Phi), \tag{10}$$

where $I(t)$ is the current at time t, I_A is the current amplitude, and Φ is phase angle by which the potential lags the current. According to the Ohm's law the impedance is defined as the ratio of potential and current

$$Z = \frac{E(t)}{I(t)}. \tag{11}$$

Impedance has magnitude ($Z_0 = \frac{E_0}{I_0}$) and phase angle. Therefore it is convenient to present the impedance as:

$$Z = Z_A\left(\cos \Phi + \sqrt{-1} \sin \Phi\right) = Z' + \sqrt{-1}Z'', \tag{12}$$

where Z' is real part of impedance and Z'' the imaginary part of the impedance [123].

If a sinusoidal potential is applied to a pure resistor with resistance R, then $Z_0 = R$ and $\Phi = 0°$ for all frequencies.

However, if a sinusoidal potential is applied across a pure capacitor, the impedance can be calculated according to the relationship

$$Z = \frac{1}{\sqrt{-1}\omega C} = -\frac{\sqrt{-1}}{\omega C}, \tag{13}$$

where C is the differential capacitance and the phase angle is $\Phi = -90°$, *i.e.* the impedance depends on the frequency and is completely imaginary. The magnitude of the impedance for a pure capacitor is [123]:

$$Z_0 = \frac{1}{\omega C}. \tag{14}$$

In the case of serial combination of resistor and capacitor, the currents through both elements are the same. Hence, the total impedance can be calculated from [123]:

$$Z = R - \frac{\sqrt{-1}}{\omega C}. \tag{15}$$

4.8. *In situ* study of the adsorbed monolayers on single crystal electrodes

The application of STM in various scientific fields has added a great amount of knowledge and understanding through enabling the real space imaging of molecules on solid surfaces. Molecular imaging clarifies the arrangements of particles in arrays, orientations and even in intramolecular structures in ambious, UHV and solution conditions. The visualisation of adsorbed layers on well-defined single crystal surfaces has received much attention in the last decade due to their significance in surface and materials science, interfacial electrochemistry and nanotechnology, such as ordered adsorption, island nucleation and growth, surface reconstruction and molecular electronics. Furthermore, directly connected to the interfacial phase formation processes are kinetic phenomena, such as catalytic activity and chirality of surfaces, selective recognition of molecular functions, and oscillating chemical reactions.

Pairing supramolecular chemistry and scanning probe microscopy allows the visual consideration of molecular self-assembly in sub-molecular space [124].

The two-dimensional (2D) structure and reactivity of organic, ionic, or metallic (sub-)monolayers can also be studied at potentiostatically controlled electrode | electrolyte interfaces. This approach has the advantage over a non-electrochemical environment that the structural and dynamic properties of the adsorbate and the working electrode can be directly altered by changing the applied electrode potential [25].

The electrochemical adsorption of organic molecules depends on numerous aspects: 1) on the interactions with the electrode through image charges and/or substrate-adsorbate coordination; 2) on the displacement of previously adsorbed solvent molecules and/or electrolyte ions; 3) on the hydrophobic and hydrophilic interactions with remaining solvent molecules; 4) on the interactions between the adsorbate species. The latter may involve dispersion and dipole-dipole coupling, π-stacking, and/or hydrogen bonding [44].

The first electrochemical studies of 2D phase transitions, *e.g.* the formation of compact monolayers of organic molecules or salts, were performed at ideally smooth Hg(*hkl*) electrodes [125,126]. The use of well-defined single crystal electrodes, such as Au(*hkl*), Pt(*hkl*), and Cu(*hkl*), demonstrated the considerable influence of the electrode chemical composition and surface structure (crystallographic orientation, defects, *etc*.) on electrode kinetics and 2D phase transitions in electrochemically formed adlayers of organic molecules [27,44,127,128], ions [129], or metals [130]. Also additional contributions arise from solvent molecules and the co-adsorption of ions of the supporting electrolyte.

The combination of classical electrochemical experiments, based on measurements of current, charge density or impedance as a function of the applied electrode potential or time, with structure-sensitive *in situ* techniques, such as STM and atomic force microscopy [28,41–44,127,131–134], surface X-ray scattering [135], and/or vibrational spectroscopies (SEIRAS [42,45], Raman [136,137], *etc*.) complemented by density functional theory calculation methods [138–141] provide an approximate understanding of the solid | liquid interfaces in macroscopic and microscopic (molecular or atomic) levels. Applying the knowledge gathered it is possible to develop the general molecular theory taking into account the influence of the crystallographic structure, electronic and chemical nature of the surface as well as the adsorption properties (molecular structure, dielectric properties and polarisability, charge density localisation) on the 2D condensation phenomenon [25].

5. EXPERIMENTAL

The surface of the basal Cd(0001) plane was prepared by electrochemical polishing in a hot (80 °C) 1:1 solution of concentrated phosphoric acid (Lachner, 85.0%) and Milli Q^+ water at current density $i \approx 1.48$ A cm^{-2}. The surface of Sb(111) has been prepared by electrochemical polishing in 10:1 saturated aqueous KI (Sigma, 99.5%) + concentrated HCl (Fluka Analytical, $\geq$ 37.0%) solution at a current density $i \approx 1.45$ A cm^{-2}.

For studying the Cd(0001) plane in aqueous electrolyte the electrochemically polished electrode was submerged into the 0.1 M Na_2SO_4 + 1.0×10^{-5} M H_2SO_4 aqueous solution (previously saturated with Ar (99.999%)) at electrode potential $E = -1.10$ V *vs.* Ag | AgCl in saturated KCl aqueous solution. The self-made hermetic three-electrode cell with large Pt auxiliary electrode and Ag | AgCl sat. KCl reference electrode, connected to the *in situ* STM cell through Luggin capillary, was used. The region of ideal polarisability (-1.30 V $\leq E \leq -0.90$ V *vs*. Ag | AgCl sat. KCl) was established using CV and EIS methods (Autolab PGSTAT 30 with FRA II system). The series capacitance (C_S) values were measured at constant fixed frequency (mainly at $f = 210$ Hz).

For studying the Cd(0001) and Sb(111) planes in $EMImBF_4$ the electrochemically polished Cd(0001) and Sb(111) single crystal electrodes were submerged at $E = -1.10$ V and at $E = -0.60$ V *vs.* Ag | AgCl | $EMImBF_4$, respectively into the $EMImBF_4$ (Fluka Analytical, for electrochemistry, $\geq$ 99.0%, H_2O < 200 ppm), which was additionally dried inside glove box with dry Ar (99.9999%). Same electrochemical cell was used as for the aqueous electrolyte studies, but with a chlorinated silver wire quasi-reference electrode (Ag | AgCl | $EMImBF_4$). All CV and EIS measurements (using Autolab PGSTAT 320 with FRA II) were performed inside a glove box (H_2O < 1.0 ppm, O_2 < 1.0 ppm) in a three-electrode electrochemical cell. For CV measurements the potential sweep rate was varied from 5 mV s^{-1} to 100 mV s^{-1} and EIS data were measured at various fixed potentials within the ac frequency range from 0.1 Hz to 1.0×10^4 Hz.

For the *in situ* STM measurements Molecular Imaging PicoSPM™ system applying the Apiezon™ coated tungsten STM tips, prepared in our laboratory, were used. The STM-tips and measurement system were tested and calibrated using highly oriented pyrolytic graphite (HOPG) cleaved basal plane C(0001)^C (SPI™). All STM images were recorded in constant current mode with tunneling currents from 0.5 nA to 10.0 nA. For image processing and surface roughness analysis the Nanotec Electronica WSxM™ [142] and Gwyddion [143] free software products were used. Root mean square roughness (*RMS*) has been calculated using Gwyddion software from the following relation:

$$RMS = \sqrt{\frac{1}{n_d}\sum_{i=1}^{n_d} z_i^2}, \tag{16}$$

where n_d is the number of data points and z_i is the height deviation of i-th point from the mean line, defined so that the arithmetic sum of all z_i is equal to zero.

The *in situ* infrared spectra were measured using Perkin-Elmer Spectrum GX FTIR system equipped with a liquid nitrogen-cooled midrange MCT detector [69,116,144] on a 20 nm thick magnetron sputtered layer of cadmium electrode with polycrystalline surface structure. Infrared beam was directed through a ZnSe wire grid polariser and a ZnSe lens to the Si hemisphere at 65 degrees of incidence (mainly p-polarisation mode was used). SEIRAS spectra were collected during 3 minutes at a resolution of 4 cm^{-1} at fixed potential, and the measurement cycle was repeated at least 3 times. The resulting spectra were calculated by dividing the sample spectrum at fixed potential with the reference spectrum measured at reference potential and presented as absorbance A. Therefore, the positive-going bands represent a gain of a particular species at the sample potential relative to that of the background reference potential.

Aqueous solutions were prepared volumetrically using Milli Q+ water, H_2SO_4 (double distilled, Aldrich), 4,4′-BP (Fluka *purum*, 99%) and Na_2SO_4 (purified by triple recrystallisation from water and treated in vacuum to dryness). Na_2SO_4 was also calcined at 700 °C immediately prior to the measurements. The 1% 2,2′-BP (Aldrich, 99+%) and $EMImBF_4$ solutions were prepared by mass on an analytic scale.

The temperature during the experiments was kept at 24 ± 1 °C.

6. RESULTS AND DISCUSSION

6.1. Surface structure of Cd(0001) single crystal electrode in aqueous electrolyte

6.1.1. Analysis of CV and EIS data

The CV and the series capacitance *vs.* electrode potential (C_S *vs.* E) curves, given in Fig. 9 and 10, respectively, show that the Cd(0001) | 0.1 M Na_2SO_4 + 1.0×10^{-5} M H_2SO_4 interface is nearly ideally polarisable within the electrode potential region from −1.30 V to −0.90 V *vs.* Ag | AgCl sat. KCl. It can be seen that at more negative electrode potentials $|i|$ and C_S values increase, caused by the very slow cathodic hydrogen evolution at $E \leq -1.30$ V. At less negative electrode potentials a small plateau on C_S *vs.* E curve can be seen, indicating the pzc area near $E = -1.05$ V, which is in a good agreement with pzc data discussed in dilute surface inactive electrolyte solutions [54]. At more positive potentials, i and C_S values start to increase exponentially due to the anodic dissolution of Cd(0001) surface.

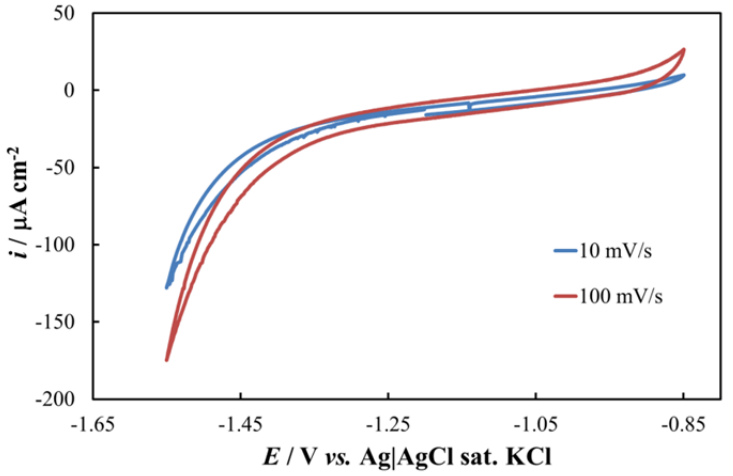

Figure 9. Current density (i) *vs.* electrode potential (E) curves measured at different scan rates (noted in figure) for Cd(0001) in 0.1 M Na_2SO_4 + 1.0×10^{-5} M H_2SO_4 aqueous solution.

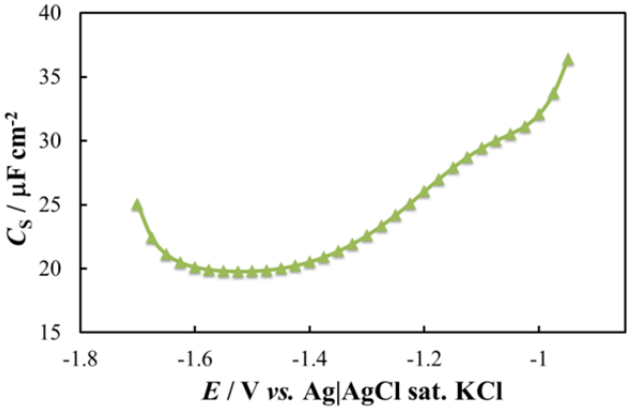

Figure 10. Series capacitance (C_S) *vs.* electrode potential (E) curve for Cd(0001) electrode in 0.1 M Na_2SO_4 + 1.0×10^{-5} M H_2SO_4 aqueous solution at 210 Hz.

From the phase angle *vs.* log f plots it can be seen that within the region of 100 Hz $< f <$ 1 Hz the absolute phase angle values are higher than 75°, describing an adsorption rate limited process (Fig. 11). At the lower ac frequencies the phase angle absolute values decrease due to the start of the very slow partial charge transfer process.

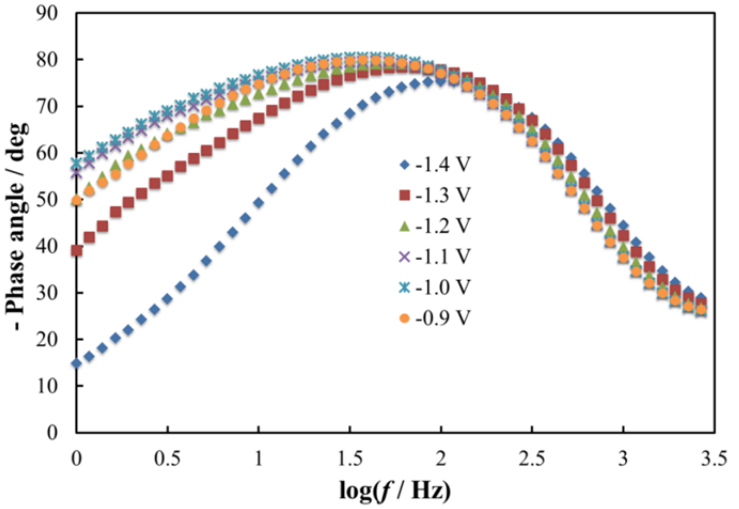

Figure 11. Phase angle *vs.* log f (frequency) plots for Cd(0001) electrode in 0.1 M Na_2SO_4 + 1.0×10^{-5} M H_2SO_4 aqueous system at different electrode potentials (*vs.* Ag | AgCl sat. KCl, noted in figure).

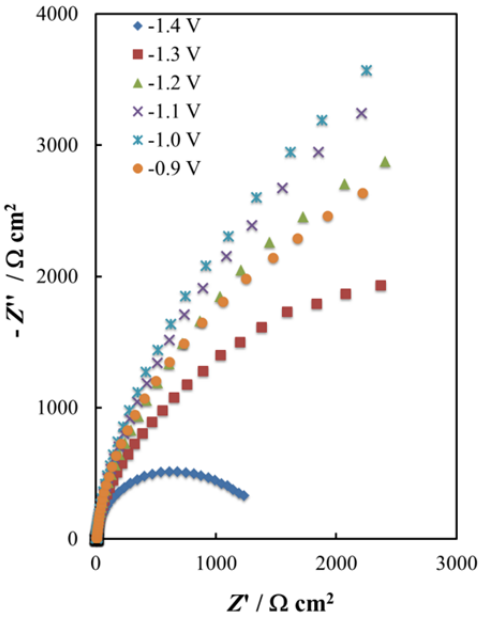

Figure 12. Complex plane plots for Cd(0001) electrode in 0.1 M Na_2SO_4 + 1.0×10^{-5} M H_2SO_4 aqueous system at different electrode potentials (*vs*. Ag | AgCl sat. KCl, noted in figure).

The Nyquist plots at different electrode potentials are presented in Fig. 12. At the smaller ac frequencies and at the pzc region the so-called capacitive behaviour prevails like in the case of Bi(111), where the very slow adsorption-desorption with partial charge transfer process from base electrolyte ions to Cd(0001) electrode surface is possible [97]. At the very low ac frequency area and at more negative electrode potentials the values of $-Z''$ and Z' decrease compared to values of $-Z''$ and Z' at potential region from −0.90 V to −1.20 V due to the start of slow cathodic process (hydrogen evolution).

6.1.2. Analysis of *in situ* STM data

According to the data given in Fig. 13a, the surface of the Cd(0001) electrode consists of atomically smooth terraces and steps with height of 5.6 ± 0.2 Å (Fig. 13b) or of multiple heights, being in accordance with Cd crystallographic data [52].

Fig. 14 shows the atomic resolution picture (a), fast Fourier transform (FFT) filtered image (b) and the surface profile (c) for the electrochemically polished Cd(0001) electrode at $E = -1.15$ V. According to these data, the regular atomic structure can be observed (with the cell parameters calculated from FFT analysis: 2.9 ± 0.3 Å). Some deviation of experimental data from crystallographic characteristics can occur due to the thermal drift distortion. The

height fluctuations observed within the region of (12×12) nm^2 plateaus exposed on Cd(0001) surface are very small, as previously shown for Bi(111) and Sb(111) electrodes [47,97].

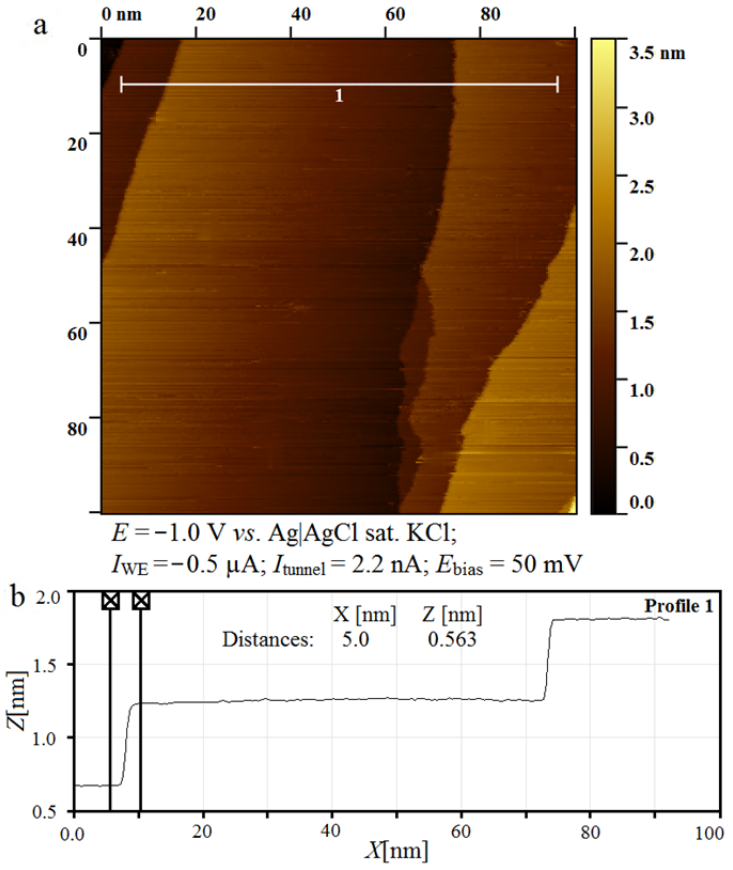

Figure 13. *In situ* STM image (a) and selected surface profile (b) for electrochemically polished Cd(0001) plane in 0.1 M Na_2SO_4 + 1.0×10^{-5} M H_2SO_4 aqueous solution at electrode potential $E = -1.00$ V *vs.* Ag | AgCl sat. KCl.

The surface structure of Cd(0001) single crystal electrode, *i.e.* the terraces and steps, is very stable during few hours within electrode potential region from −1.40 V to −0.90 V (Fig. 15a-c). This conclusion is supported by the *RMS vs. E* analysis (Fig. 15d). Therefore, in a good agreement with the CV and EIS data, there is no evidence of quick surface reconstruction of Cd(0001) surface layer as it has been established for Au(*hkl*) [59–61].

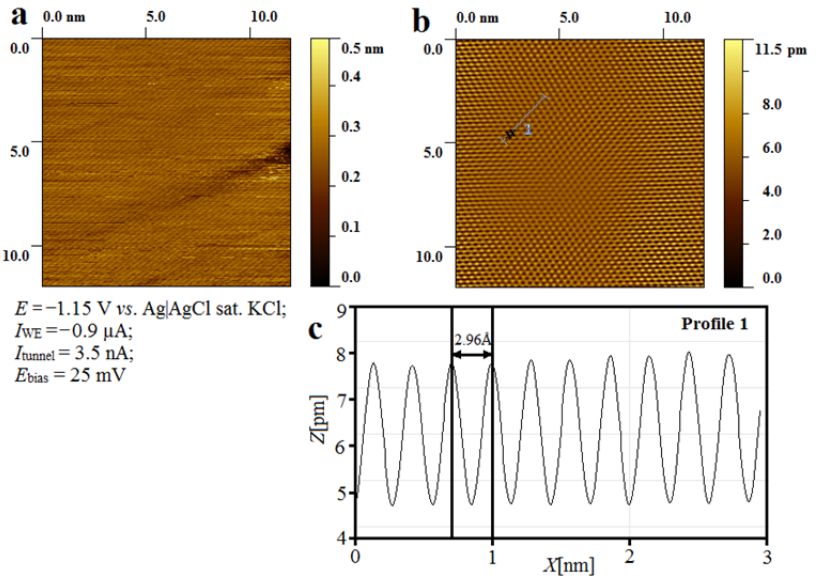

Figure 14. *In situ* STM atomic resolution image (a), FFT filtered image (b) and height profile (c) for Cd(0001) electrode in 0.1 M Na_2SO_4 + 1.0×10^{-5} M H_2SO_4 aqueous solution at electrode potential $E = -1.15$ V *vs*. Ag | AgCl sat. KCl.

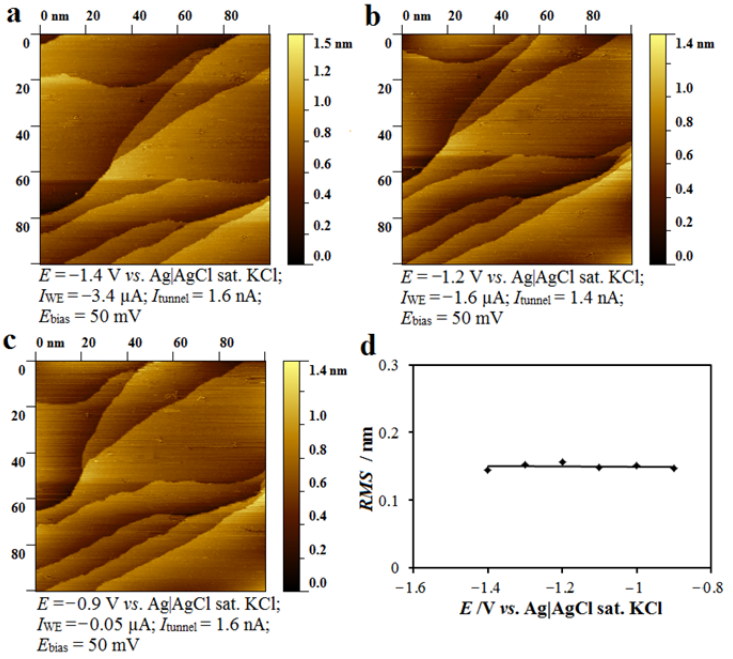

Figure 15. *In situ* STM images at various electrode potentials (noted in figure; a, b, c) and root mean square roughness (*RMS*) *vs*. fixed electrode potential (*E*) dependence (d) for Cd(0001) electrode in 0.1 M Na_2SO_4 + 1.0×10^{-5} M H_2SO_4 aqueous solution.

At less negative potentials, the surface oxidation and dissolution of the Cd(0001) electrode surface starts (Fig. 16). After holding the Cd(0001) electrodes at $E = -0.75$ V, it can be observed that some etched holes start to appear and develop on the Cd(0001) electrode surface. After some minutes the surface structure of the electrode completely changes through the dissolution of Cd(0001). The dissolution potential value established for Cd(0001) electrode is in a good agreement with the Pourbaix diagram data for polycrystalline Cd [51].

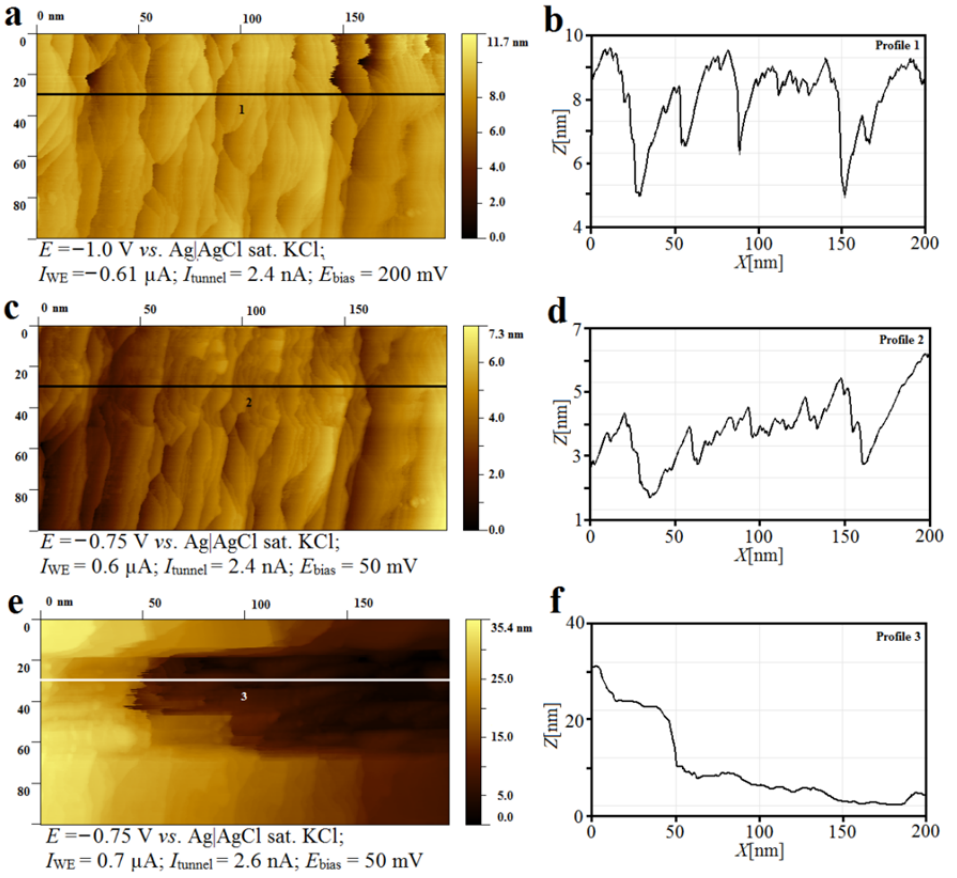

Figure 16. *In situ* STM images of Cd(0001) surface at electrode potential $E = -1.00$ V (*vs*. Ag | AgCl sat. KCl) (a) and profile (b), at $E = -0.75$ V (c) and profile (d) after 3 minutes and at $E = -0.75$ V (e) and profile (f) after 10 minutes in 0.1 M Na_2SO_4 + 1.0×10^{-5} M H_2SO_4 aqueous solution.

6.2. Adsorption of 4,4′-bipyridine at Cd(0001) surface

6.2.1. Analysis of CV and series capacitance plots

From the CV data measured for Cd(0001) | 0.1 M Na_2SO_4 + 1.0×10^{-5} M H_2SO_4 + 3.0×10^{-4} M 4,4′-BP system (Fig. 17), it can be seen that the reduction peak potential value on the CV (E_{red}) is shifting towards more negative ($|\Delta E_{red}| \geq 110$ mV) and the oxidation peak potential value (E_{ox}) towards less negative electrode potentials ($|\Delta E_{ox}| \geq 68$ mV) with the increase of the potential scan rate from 5 mVs^{-1} to 500 mV s^{-1}.

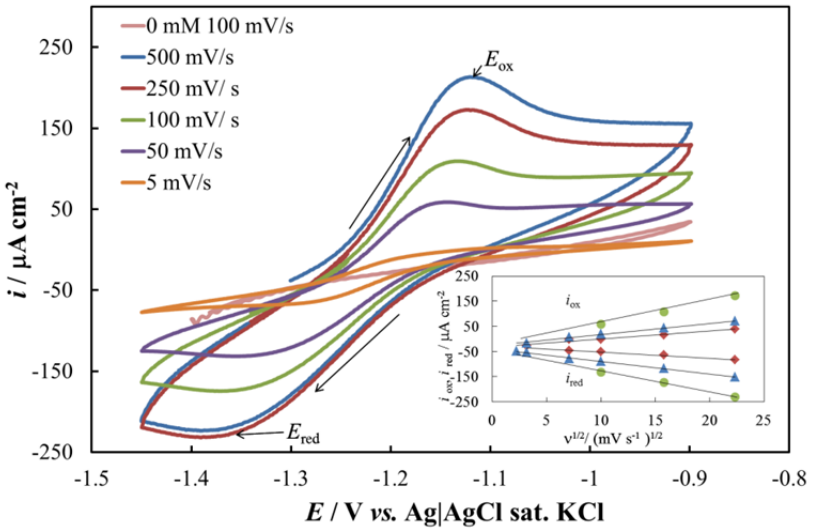

Figure 17. Current density (i) *vs.* electrode potential (E) curves for Cd(0001) in 0.1 M Na_2SO_4 + 1.0×10^{-5} M H_2SO_4 + 3.0×10^{-4} M 4,4′-BP system at various potential scan rates (noted in figure), and reduction peak current density value (i_{red}) and oxidation peak current density value (i_{ox}) dependence on square root of potential scan rate ($\sqrt{\nu}$) (inset) .

In addition, E_{red} and E_{ox} (at fixed 4,4′-BP concentration ($c_{4,4'\text{-BP}}$)) depend noticeably on the potential scan rate (Figs. 17 and 18). At fixed $\nu = 100$ mV s^{-1} $E_{ox}-E_{red} = 280$ mV (Fig. 18), indicating the quasi-reversible adsorption process of 4,4′-BP with partial charge transfer (or true faradaic charge transfer). There is a nearly linear dependence of the reduction peak current density value (i_{red}), as well as of oxidation peak current density value (i_{ox}), on $\sqrt{\nu}$ (inset in Fig. 17), demonstrating mainly mass transfer step limited processes [145–154]. However, the mass transfer (diffusion) coefficient values, which can be calculated from the slopes of i_{red} *vs.* $\sqrt{\nu}$ or i_{ox} *vs.* $\sqrt{\nu}$ plots, depend noticeably on the organic compound concentration in the solution, being lower for more concentrated 4,4′-BP solutions. This can be explained by the formation of a more compact

4,4′-BP adsorption layer on the charged Cd(0001) surface from more concentrated 4,4′-BP solutions.

Similarly to the adsorption of 4,4′-BP on the Bi(111) electrode surface [155], the current density values slightly decrease with subsequent potential sweeps (Fig. 18). The adsorption of 4,4′-BP can be considered as a quasi-reversible adsorption process (with partial charge transfer step) within the potential region investigated.

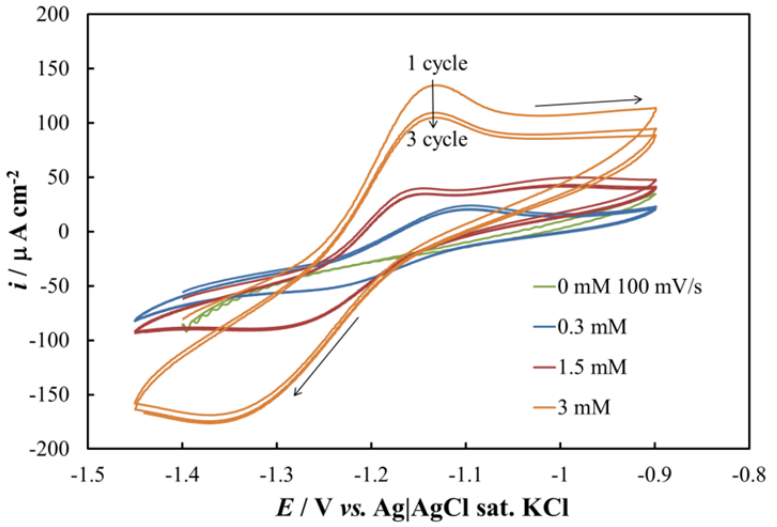

Figure 18. Current density (i) *vs.* electrode potential (E) curves for Cd(0001) electrode in 0.1 M Na_2SO_4 + 1.0×10^{-5} M H_2SO_4 + x M 4,4′-BP system (x noted in figure), at $v = 100$ mV s^{-1}.

The C_S *vs.* E curves for the Cd(0001) | 0.1 M Na_2SO_4 + 1.0×10^{-5} M H_2SO_4 + 1.5×10^{-3} M 4,4′-BP aqueous solution system were measured at different fixed ac frequencies (Fig. 19). The distinctive capacitance peak at $E = -1.20$ V can be regarded as a so-called pseudocapacitive peak, caused by the partial charge transfer process. The C_S values at $E = -1.20$ V strongly depend on f (Fig. 19), as well as on $c_{4,4'\text{-BP}}$, which is also characteristic to the adsorption of organic compounds on Hg and Bi electrodes [58−63]. The pseudocapacitive peak potential is nearly independent of $c_{4,4'\text{-BP}}$ in the solution, indicating the formation of a stable 2D structure already in very dilute 4,4′-BP solutions.

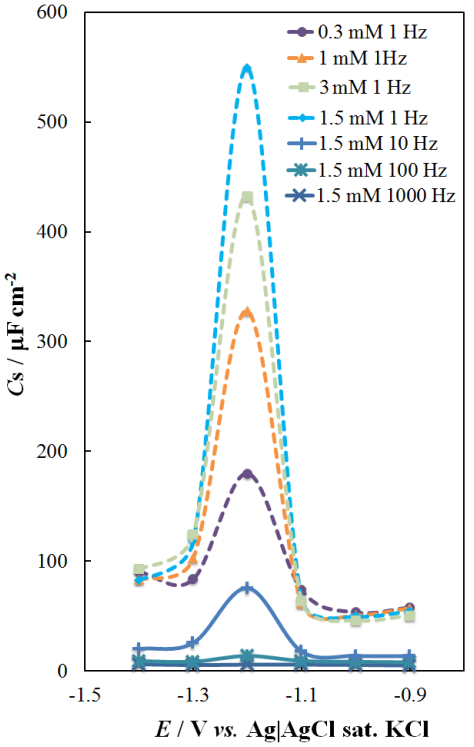

Figure 19. Series capacitance (C_S) *vs.* electrode potential (E) curves for Cd(0001) in 0.1 M Na_2SO_4 + 1.0×10^{-5} M H_2SO_4 + x M 4,4′-BP aqueous solution at various ac frequencies (noted in figure).

6.2.2. Analysis of Nyquist and Bode phase angle dependencies

The Nyquist plots for Cd(0001) | 0.1 M Na_2SO_4 + 1.0×10^{-5} M H_2SO_4 + x M 4,4′-BP systems are shown in Fig. 20. Reduction of the 4,4′-BP layer and faradaic electroreduction processes take place at $E \leq -1.40$ V. There are no linear areas with the slope values varying from 45° to 60° in the Nyquist plots, characteristic of the finite length mass transfer step limited adsorption processes at $f < 10$ Hz.

The high and low frequency maxima (100 – 150 Hz; 0.4 − 0.3 Hz) in the Bode phase angle plots for Cd(0001) | 0.1 M Na_2SO_4 + 1.0×10^{-5} M H_2SO_4 + x M 4,4′-BP systems (Fig. 21) can be characterised by the distinctly different characteristic relaxation times. Therefore two parallel processes are suggested: slow adsorption (with following partial charge transfer step) and true faradaic oxidation processes at $E \geq -0.90$ V.

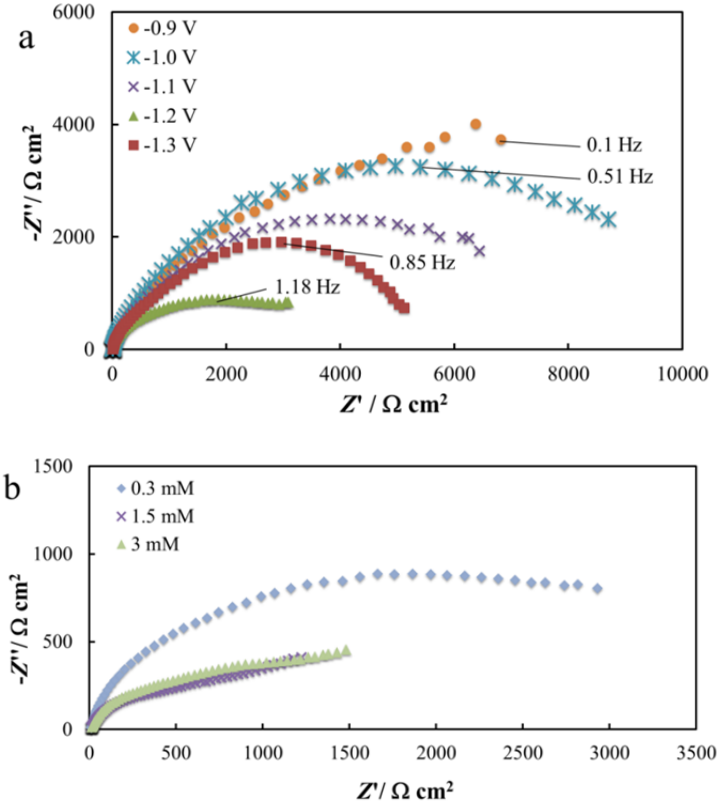

Figure 20. Nyquist ($-Z''$,Z') plots for Cd(0001) electrode in 0.1 M Na_2SO_4 + 1.0×10^{-5} M H_2SO_4 + x M 4,4′-BP aqueous solution at different electrode potentials (*vs.* Ag | AgCl sat. KCl, noted in figure) and x: 3×10^{-4} M (a); and for different 4,4′-BP concentrations (noted in figure) at $E = -1.20$ V *vs.* Ag | AgCl sat. KCl (b).

At more negative electrode potentials ($E = -1.40$ V), the region of intensive decrease in the absolute value of phase angle is shifted towards higher f values with the increase of negative polarisation (Fig. 21a), which could be explained by the reductive desorption of 4,4′-BP from the Cd(0001) | electrolyte interface [136,156].

The phase angle values strongly depend on the $c_{4,4'\text{-BP}}$ in solution at $E = -1.20$ V (Fig. 21b). The quick adsorption layer formation, *i.e.* less negative phase angle values at higher ac frequencies (followed by the slower partial charge transfer step at $f < 1.0$ Hz), has been verified for the most concentrated 4,4′-BP solutions ($c_{4,4'\text{-BP}} \geq 1.5\times10^{-3}$ M).

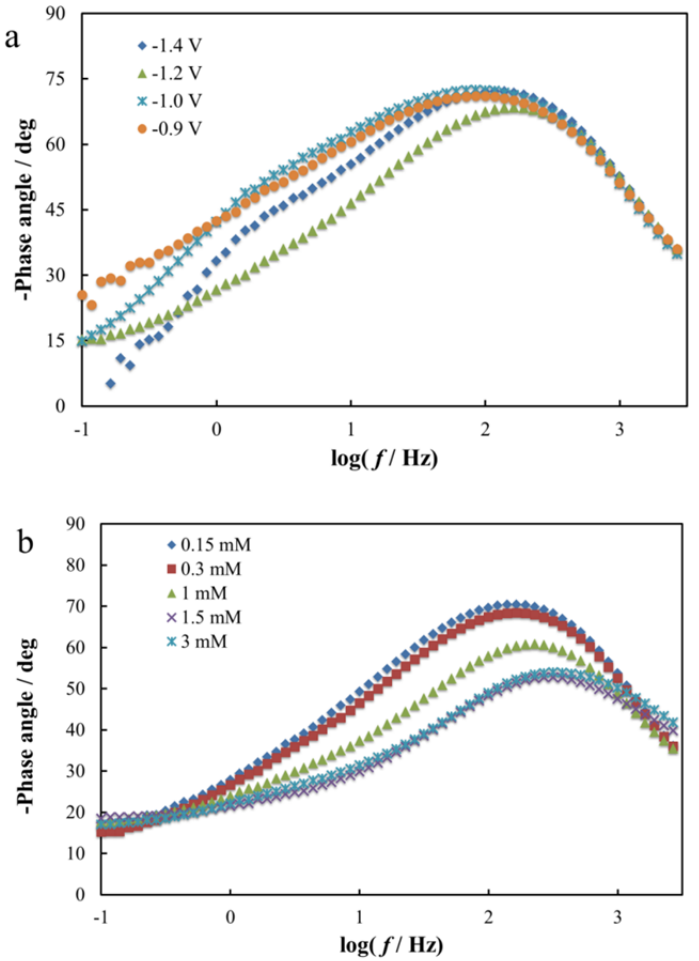

Figure 21. Bode phase angle *vs.* log *f* (frequency) plots for Cd(0001) electrode in 0.1 M Na_2SO_4 + 1.0×10^{-5} M H_2SO_4 + *x* M 4,4′-BP aqueous solution at different electrode potentials (*vs*. Ag | AgCl sat. KCl, noted in figure) and *x*: 3×10^{-4} M (a); and for different 4,4′-BP concentrations at $E = -1.20$ V *vs*. Ag | AgCl sat. KCl (b) (noted in figure).

6.2.3. Analysis of *in situ* STM data

It has been established that in 0.1 M Na_2SO_4 + 1.0×10^{-5} M H_2SO_4 + 1.5×10^{-3} M 4,4′-BP and at $E = -1.25$ V (*vs.* Ag | AgCl in sat. KCl) 4,4′-BP molecules form a stripe pattern on the Cd(0001) electrode surface (Fig. 22a). Similar patterns have been observed on the Au(111) [27,44], Bi(111) [155] and Cu(111) [127] electrodes, where the commensurate structures of the 4,4′-BP molecules are formed by translation and rotation of the molecules towards the surface [26,134].

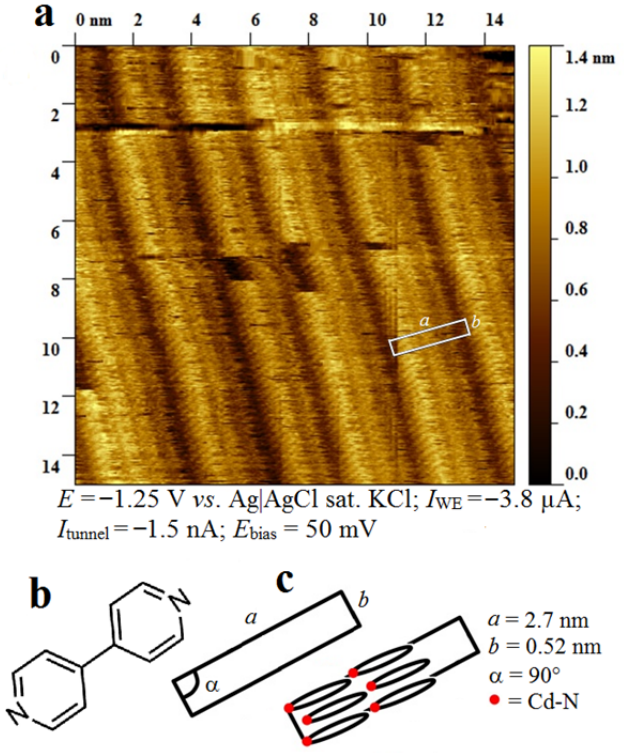

Figure 22. *In situ* STM image for 4,4′-BP adsorption on Cd(0001) electrode from 0.1 M Na_2SO_4 + 1.0×10^{-5} M H_2SO_4 + 1.5×10^{-3} M 4,4′-BP aqueous solution at $E = -1.25$ V *vs.* Ag | AgCl sat. KCl (a), chemical structure of 4,4′-BP (b) and proposed packing model for adsorbed 4,4′-BP molecules and calculated cell dimensions (c).

In Fig. 22a the high-resolution *in situ* STM image for 4,4′-BP adsorption from 0.1 M Na_2SO_4 + 1.0×10^{-5} M H_2SO_4 + 1.5×10^{-3} M 4,4′-BP to the Cd(0001) surface is given. The periodic arrays of bright features are clearly visible at tip bias potential E_{bias} = 50 mV and at tunneling current $I_{tunnel} = -1.50$ nA. From the *in situ* STM image the characteristic dimensions for the unit cell of the adsorption layer have been measured: a = 2.70 nm, b = 0.52 nm and α = 90° (Fig. 22b). Based on the values of a, b, and the angle α, a rectangular unit cell for the co-adsorbed 4,4′-BP and hydrated sulphate ions forming the adlayer at the Cd(0001) | 4,4′-BP + 0.1 M Na_2SO_4 + 1.0×10^{-5} M H_2SO_4 interface has been proposed. Based on the unit cell parameters, the approximate 4,4′-BP adlayer coverage 4.7×10^{-10} mol cm^{-2} has been calculated.

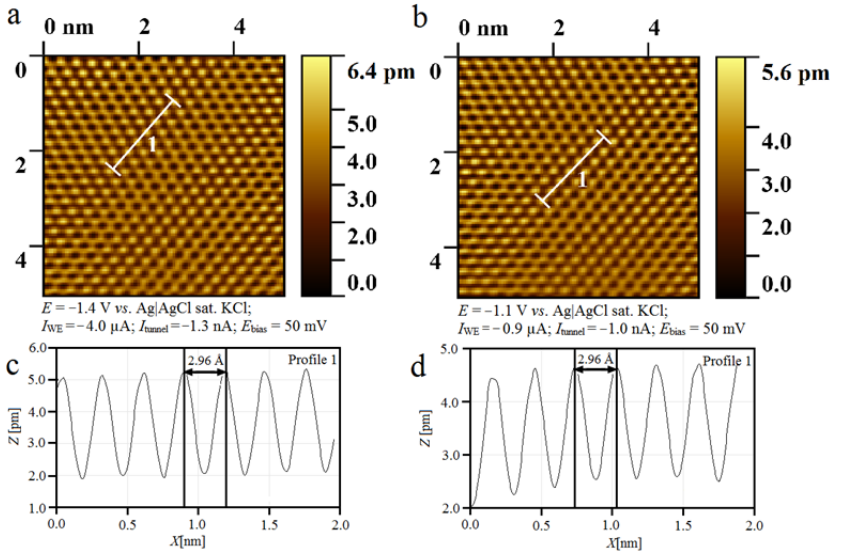

Figure 23. Fast Fourier transform filtered *in situ* STM images (a, b) and selected surface profiles (c, d) for electrochemically polished Cd(0001) plane in 0.1 M Na_2SO_4 + 1.0×10^{-5} M H_2SO_4 + 1.5×10^{-3} M 4,4′-BP aqueous solution at electrode potential $E = -1.10$ V *vs*. Ag | AgCl sat. KCl (a, c) and at $E = -1.40$ V (b, d).

It is interesting that the strongly adsorbed compact layer structures on Cd(0001), detectable by *in situ* STM method, form only within the very limited region of potentials, from −1.25 V to −1.30 V and at lower 4,4′-BP concentrations ($c_{4,4'\text{-BP}} = 1.5\times10^{-3}$ M). The compact 4,4′-BP monolayer dissolves when the potential of Cd(0001) electrode is swept from $E = -1.30$ V towards more negative values, in agreement with EIS data. The compact adsorption layer cannot be visualised at $E > -1.25$ V (using the *in situ* STM) probably due to the very compact nature of the adsorbed 4,4′-BP layer and strong chemical bonding of the adsorbed molecules on Cd(0001) surface (including partial charge transfer step). However, no structural changes were observed in the adsorbed layer, while cycling the electrode potential during a long time within $-1.30\text{ V} \le E \le -1.25$ V. At $E \le -1.35$ V and $E > -1.25$ V, the atomic resolution level picture, characteristic of the inactive supporting 0.1 M Na_2SO_4 + 1.0×10^{-5} M H_2SO_4 electrolyte | Cd(0001) interface (Fig. 23), was visualised.

6.2.4. Analysis of surface enhanced infrared reflection absorption spectroscopy data

In situ SEIRAS measurements were applied to identify the 4,4′-BP adsorption as well as the orientational changes in the adsorbed 4,4′-BP + HSO_4^- or SO_4^{2-}

anions layer structure. The SEIRAS spectra for thin-layer cadmium electrode (Fig. 24) demonstrate structural changes in the first few monolayers adsorbed at the Cd | 0.1 M Na_2SO_4 + 1.0×10^{-5} M H_2SO_4 + 1.5×10^{-3} M 4,4′-BP aqueous solution interface whilst variating the applied electrode potential.

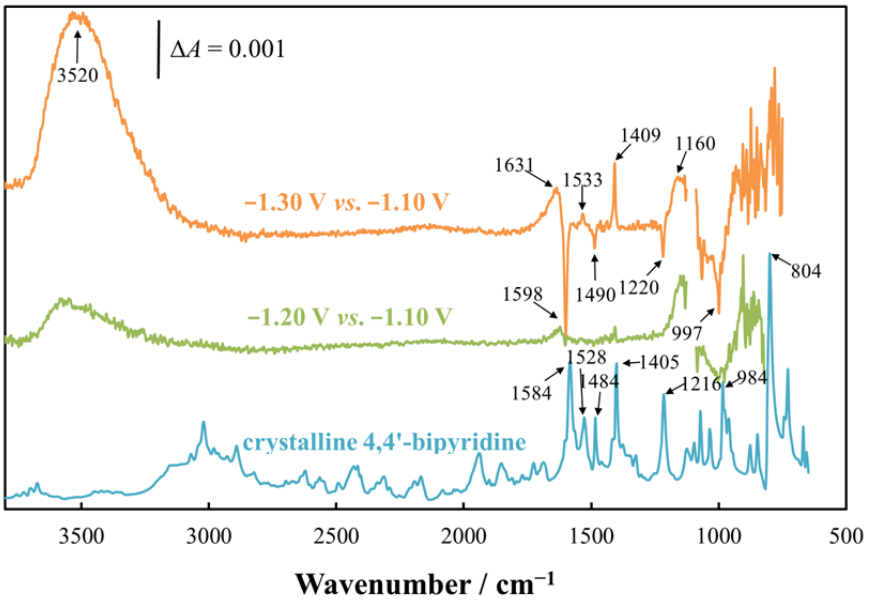

Figure 24. SEIRAS spectra for Cd film electrode in 0.1 M Na_2SO_4 + 1.0×10^{-5} M H_2SO_4 + 1.5×10^{-3} M 4,4′-BP aqueous solution at different electrode potentials (background spectra were measured at $E = -1.10$ V *vs.* Ag | AgCl sat. KCl).

The potential modulation technique has been applied to measure the spectra and a potential near the pzc ($E = -1.10$ V *vs.* Ag | AgCl sat. KCl) [157–159] has been used as the reference potential against which all potential induced changes at the interface have been compared.

The SEIRAS data show that there are large spectral changes within applied electrode potential region from −1.20 V to −1.30 V, *i.e.* within the same potential region where the so-called pseudocapacitance maximum has been shown *via* CV and EIS methods. The spectrum measured at $E = -1.20$ V mainly shows the weak absorption bands that are characteristic of changes within the electrical double layer. The spectrum at $E = -1.30$ V shows extremely strong absorption bands characteristic of large-scale interfacial interaction changes. Thus, increase in the amount of crystalline water at the interface (seen by the broad H-bonded water absorption bands at 3520 and 1630 cm^{-1}) and a decrease in the amount of 4,4′-BP at the Cd electrode | 0.1 M Na_2SO_4 + 1.0×10^{-5} M H_2SO_4 + 1.5×10^{-3} M 4,4′-BP aqueous solution interface have been established.

Interestingly, it can be seen that the bands representative of the molecular vibrations parallel to the longitudinal axis of the neutral 4,4′-BP molecule (bands at 1598, 1490, 1220 and 997 cm^{-1}) are strongly negative, while the bands representative of vibrations perpendicular to this axis are weakly positive (bands at 1533 and 1409 cm^{-1}). Therefore, as seen from the CV and EIS experiments, there is indeed a slight decrease in the interfacial concentration of 4,4′-BP at more negative electrode potentials (at $E = -1.30$ V) being replaced by the well-ordered (so-called crystalline) water structure and electrolyte ions (sulphate band at 1160 cm^{-1}).

On the other hand, it was also established that the orientation of the adsorbed 4,4′-BP molecules on Cd electrode changes relative to the pzc. While the molecules are likely perpendicular (similar to that shown for the Au(111) interface [160] due to end-on bonding) to the surface at the Cd electrode at pzc (seen by strong absorption bands along the longitudinal axis of the molecule, perpendicular to the surface), their orientation is shifted towards a more parallel orientation to the metal | solution interface at more negative electrode potentials.

SEIRAS measurements also confirm that the faradaic reduction process at $E \leq -1.40$ V corresponds to the reduction of 4,4′-BP molecules, similar to what has been established by previous *in situ* Raman measurements [136,156].

6.2.5. Discussion of the properties of the Cd(0001) | 4,4′-bipyridine interface

The results of the CV and EIS data for the Cd(0001) 0.1 M Na_2SO_4 + 1.0×10^{-5} M H_2SO_4 + 4,4′-BP interface indicate that there are two specific applied potential areas, where the adsorption and the formation of 2D 4,4′-BP monolayer takes place.

At less negative electrode potentials, $E \geq -1.20$ V, 4,4′-BP adsorbs forming densely packed stripes. Comparable results have been shown for the Au(111) | 4,4′-BP + supporting electrolyte interface, where the 4,4′-BP molecules are adsorbed head-on through a metal-nitrogen bond [160]. Unfortunately, to detect this structure with *in situ* STM, extremely low tunneling currents are necessary in order to not saturate the through-molecule tunneling, which has been very difficult even for the Au(111) | 4,4′-BP interface [160].

At more negative electrode potentials ($E \leq -1.25$ V) some of the 4,4′-BP molecules desorb, giving rise to a reorientation peak in the CVs as well as the so-called pseudocapacitive peak in the C_S *vs*. E curve. As the surface coverage of the organic adlayer of 4,4′-BP decreases ($E = -1.25$ V), a striped structure is formed on the Cd(0001) plane structure, clearly seen on *in situ* STM images. From the *in situ* STM images it was determined that the fine structure parameters for the formed layer are: 2.70 nm between the stripes and 0.26 nm in the direction of the stripes (between adsorbed 4,4′-BP molecules). These parameters were used to formulate an adsorption unit cell. It is also seen from

the *in situ* STM data, that at $E < -1.20$ V, the entire surface is not covered with an ordered organic adsorption layer. The calculated adlayer coverage is about 4.7×10^{-10} mol cm^{-2}.

In situ SEIRAS measurements were performed to identify the adsorbate molecules as well as the influence of the surface potential to the orientation of the adsorbed 4,4′-BP molecules. The SEIRAS results indicate that the 4,4′-BP is adsorbing on Cd(0001) in the molecular form and not as on acidic radical found for the Bi(111) | 4,4′-BP + acidified surface inactive electrolyte system [155]. The results also indicate that at more negative electrode potentials the 4,4′-BP molecules are probably orientated nearly parallel to the Cd(0001) surface and in a more reclined position relative to the orientation near the pzc.

In order to extend the understanding of the adlayer structure, *i.e.* the orientation of the organic molecules, modelling of the interfacial structure was conducted using the data from *in situ* STM and SEIRAS measurements (Fig. 25). It was determined that the parameters for the unit cell nearly correspond to the distances within the metal cluster ($d = 0.27$ nm). Therefore, presumably the bonds between the metal and nitrogen atoms remain stable even when the surface concentration of 4,4′-BP molecules changes. Different adlayer structures were tested and evaluated based on both optimal packaging density and minimal energy values. The best fitting results were also evaluated against the *in situ* STM results until a reasonable fit was found.

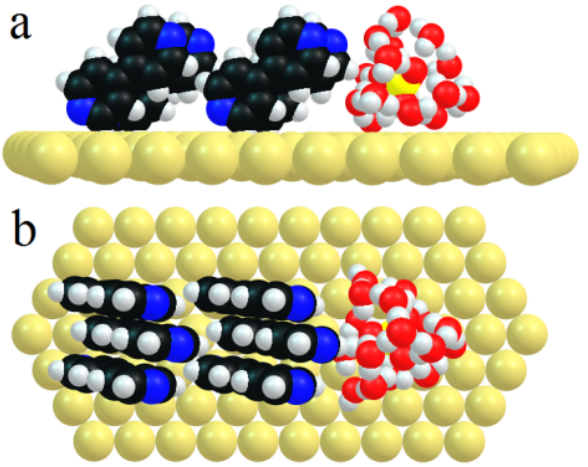

Figure 25. Models illustrating 4,4′-BP and hydrated sulphate ions on the Cd(0001) surface from the side (a) and from above (b).

6.3. Surface structure of Cd(0001) single crystal electrode in 1-ethyl-3-methylimidazolium tetrafluoroborate ($EMImBF_4$)

6.3.1. Analysis of *in situ* STM data

According to the *in situ* STM data given in Fig. 26, the surface of the electrochemically polished Cd(0001) electrode in $EMImBF_4$ consists of atomically smooth terraces which are separated by monoatomic steps of medium height 5.6 ± 0.3 Å (Fig. 26b) (or of multiple heights). The heights of the steps are in a good agreement with the data for Cd crystallographic structure.

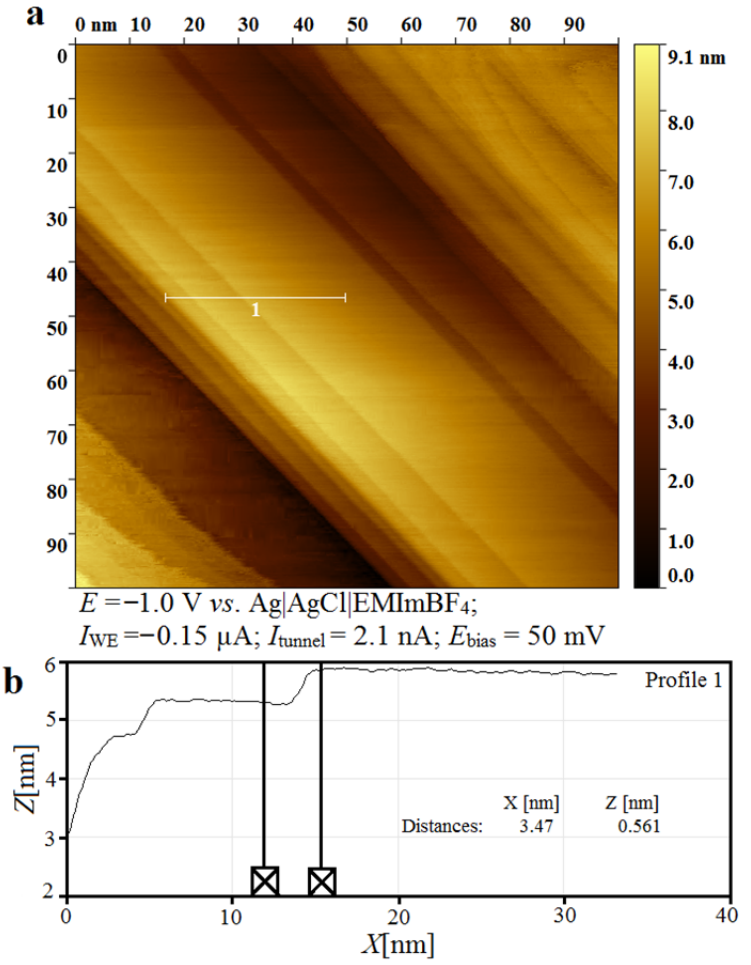

Figure 26. *In situ* STM image (a) and selected surface profile (b) for electrochemically polished Cd(0001) plane in $EMImBF_4$ at $E = -1.00$ V *vs.* Ag | AgCl | $EMImBF_4$.

The data given in Fig. 27 show the atomic resolution picture with an inset of a fast Fourier transform (FFT) filtered image of the raw data (Fig. 27a) and selected surface profile (Fig. 27b) for the Cd(0001) electrode at $E = -1.15$ V. On these images the regular atomic structure of Cd(0001) can be seen with the interatomic distances measured from FFT analysis: 2.9 ± 0.3 Å, which is in conformity with crystallographic data of cadmium ($a = 2.9793$ Å [52]).

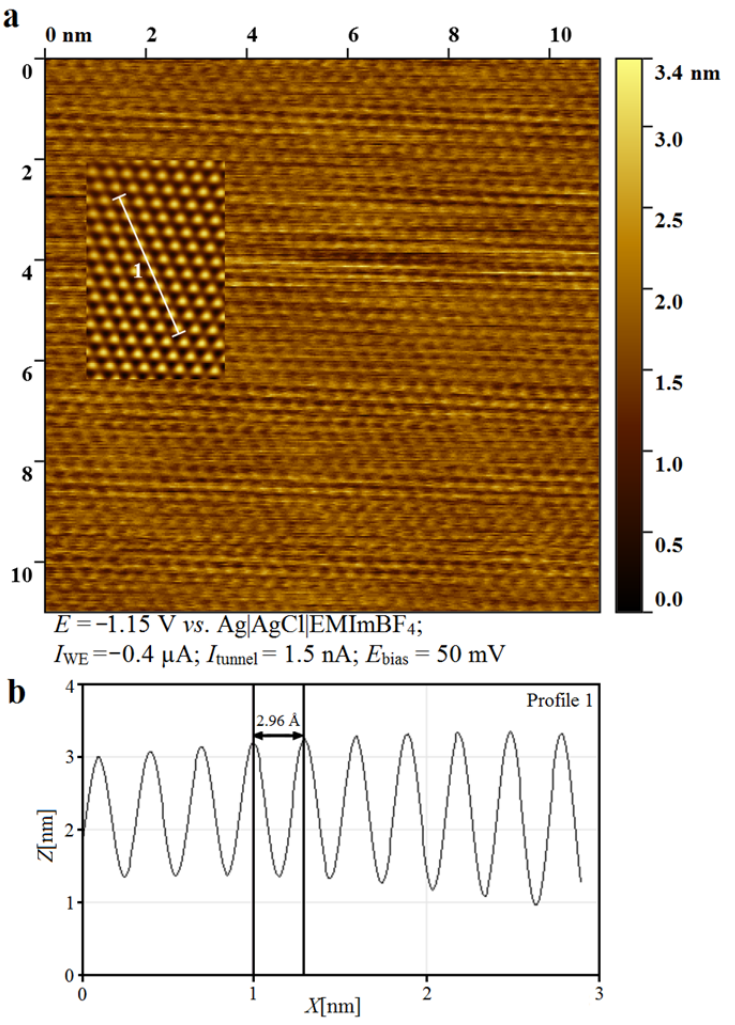

Figure 27. *In situ* STM atomic resolution image with a fast Fourier transform filtered image inset (a) and height profile (b) for Cd(0001) plane in $EMImBF_4$ at $E = -1.15$ V *vs*. Ag | AgCl | $EMImBF_4$.

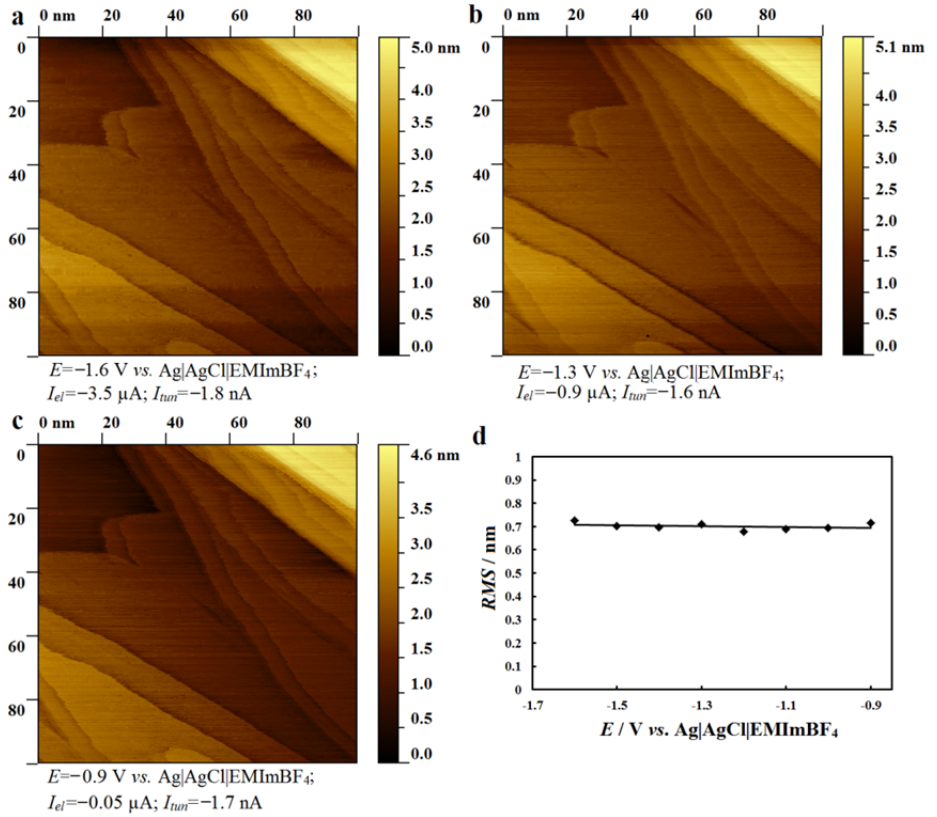

Figure 28. *In situ* STM images at various electrode potentials (*E*) *vs*. Ag | AgCl | $EMImBF_4$ (noted in figure; a, b, c) and root mean square roughness (*RMS*) *vs*. *E* dependence (d) for Cd(0001) electrode in $EMImBF_4$.

The structure of nanometric terraces separated by the steps is very stable during several hours within potential region from −1.60 V to −0.90 V (Fig. 28a-c). *RMS vs*. electrode potential dependence (Fig. 28d) has been analysed to confirm this conclusion. Therefore, it can be concluded that no quick surface reconstruction of the Cd(0001) surface layer is taking place at the electrode | ionic liquid interface as it has been established for Au(*hkl*) single crystal electrode [161–163].

6.3.2. Analysis of CV and EIS data

CVs (Fig. 29) were measured within a potential region from −1.60 V to −0.90 V (*vs*. Ag | AgCl | $EMImBF_4$). Based on the data in Fig. 29, there are no surface oxidation or reduction peaks in the CVs, but the values of |*i*| are rather high due to relatively cathodic potentials for a *sp*-metal Cd(0001) electrode, where several decomposition processes might start.

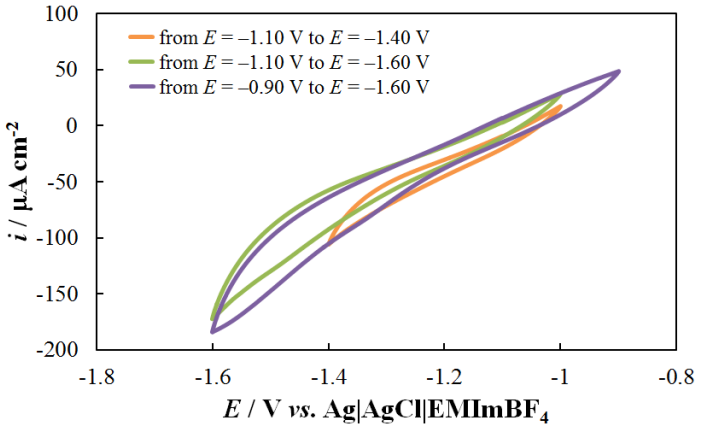

Figure 29. Current density (*i*) *vs.* electrode potential (*E*) curves for Cd(0001) in $EMImBF_4$ at potential scan rate 10 mVs^{-1}.

According to the C_S *vs. E* curves measured at 210 Hz (Fig. 30), capacitance values increase at more positive and negative electrode potentials. The lowest values of C_S were measured at $E = -1.35$ V. The system is very stable in time, as the time gap for curves 1 and 2 (Fig. 30) is approximately 24 h, but the capacitance values differ less than 5%. There is very limited hysteresis in the C_S *vs. E* curves, which are measured first forward positive (curve 2) and thereafter negative direction (curve 3). This indicates that the slow rate partial charge transfer processes are nearly reversible.

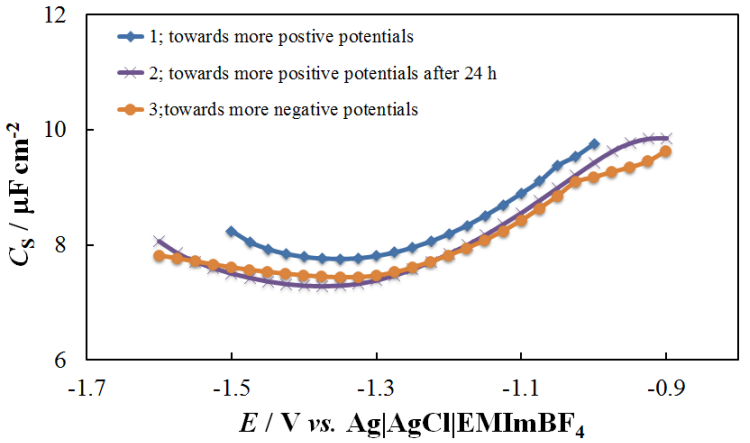

Figure 30. Series capacitance (C_S) *vs.* electrode potential (*E*) dependencies for Cd(0001) in $EMImBF_4$ at 210 Hz.

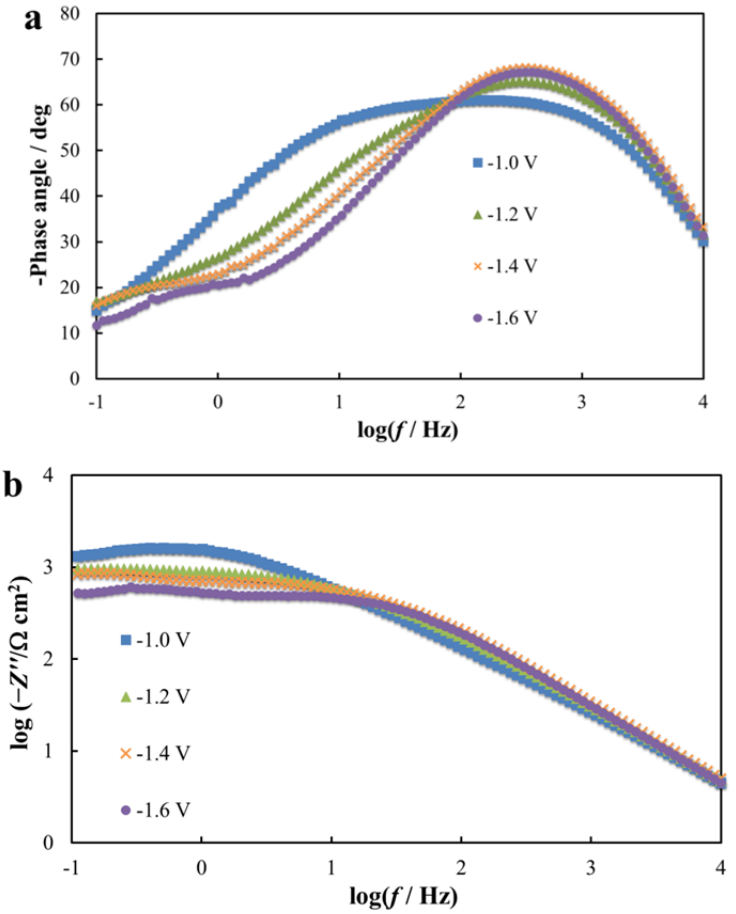

Figure 31. Phase angle *vs*. log *f* (a) and log −*Z*″ *vs*. log *f* (b) dependencies for Cd(0001) in $EMImBF_4$ at various potentials *vs*. Ag | AgCl | $EMImBF_4$ (noted in figure).

The measured EIS data (Fig. 31) indicate slow adsorption processes with the partial charge transfer processes at all potentials measured. This kind of behaviour is different from data measured for Bi single crystal electrode in $EMImBF_4$, where there are no slow partial charge transfer or faradaic processes at Bi(111) | $EMImBF_4$ interface within electrode potential region from −1.10 V to −0.20 V (*vs*. Ag | AgCl | $EMImBF_4$) [164]. Considering the shape of the phase angle *vs*. log *f* plots (Fig. 31a) a deviation from an ideally polarisable interface can be seen at low and very low frequencies. At lower frequencies both adsorption and partial charge transfer (or faradaic) processes between the electrode surface and adsorbed species take place. Some traces of water and oxygen can be found in $EMImBF_4$ and they can be reduced at Cd(0001) surface. The H_2O adsorption is possible on the surface of Cd(0001) during the electrochemical polishing in an aqueous solution, as Cd is a highly hydrophilic

metal [37]. Based on the shape of the log $-Z''$ *vs*. log f (Fig. 31b) curves, it can be concluded that at $f > 50$ Hz the electrical double layer formation kinetics depend weakly on potential applied and nearly ideal polarisability can be seen, but at lower frequency range mixed kinetic processes occur.

6.4. Surface structure of Sb(111) single crystal electrode in $EMImBF_4$

6.4.1. Analysis of *in situ* STM data

According to the *in situ* STM data (Fig. 32a-c), the surface of the electrochemically polished Sb(111) electrode consists of atomically smooth terraces.

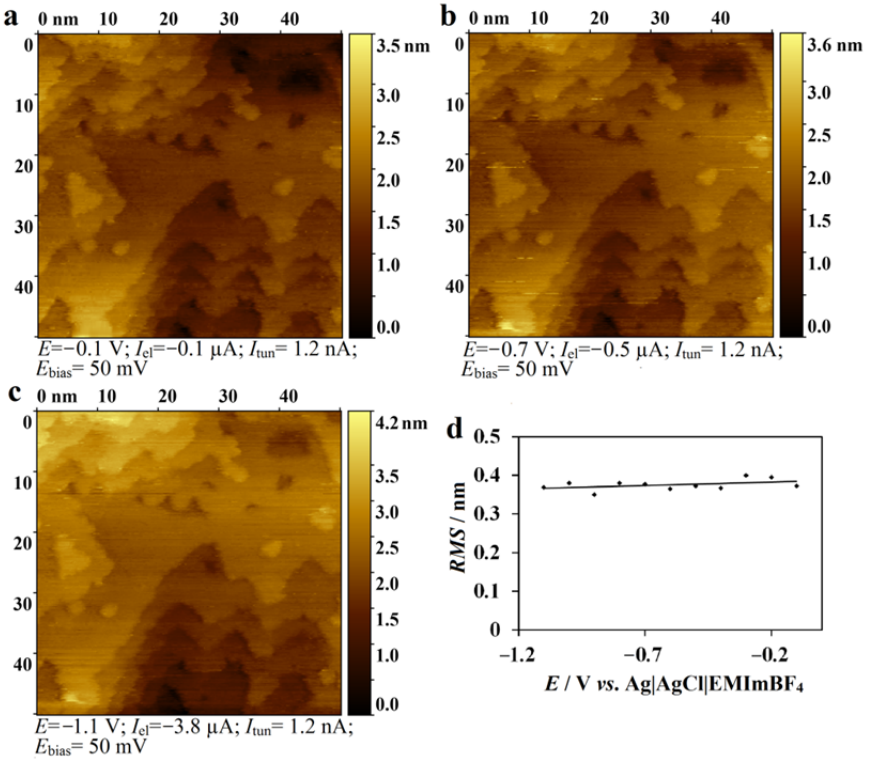

Figure 31. *In situ* STM images at various electrode potentials (E) *vs*. Ag | AgCl | $EMImBF_4$ (noted in figure; a, b, c) and root mean square roughness (*RMS*) *vs*. E dependence (d) for Sb(111) electrode in $EMImBF_4$.

The surface structure of Sb(111) in $EMImBF_4$ is very stable during several hours whilst the surface potential is scanned within the potential region from −1.10 V to −0.10 V (Figs. 32a-c), similarly to Sb(111) surface in surface

inactive aqueous electrolyte solution [47]. *RMS vs*. *E* dependence analysis (Fig. 32d) affirmed this conclusion. Thus, similarly to Cd(0001) single crystal electrode in $EMImBF_4$, there is no quick surface reconstruction of the Sb(111) surface layer as it has been established for Au monocrystalline electrodes [161–163].

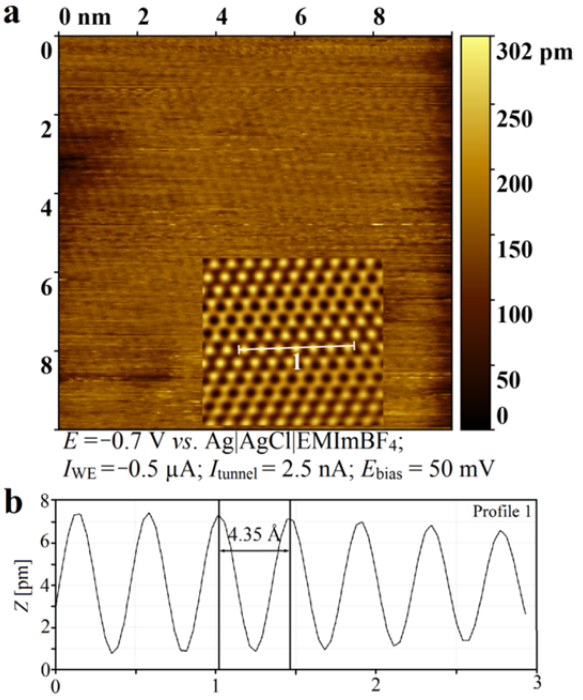

Figure 33. *In situ* STM atomic resolution image with a FFT filtered image inset (a) and corresponding height profile (b) for Sb(111) electrode in $EMImBF_4$ at electrode potential $E = -0.70$ V *vs*. Ag | AgCl | $EMImBF_4$.

The data given in Fig. 33a show the atomic resolution image with a fast Fourier transform (FFT) filtered image (inset in Fig. 33a) and surface profile (Fig. 33b) for the Sb(111) electrode at $E = -0.70$ V. On these images the regular atomic structure can be seen with the interatomic distances 4.3 ± 0.3 Å calculated from FFT analysis, being in a good agreement with Sb(111) crystal structure data (a = 4.3084 Å [56,57]).

6.5.1. Analysis of CV and EIS data

The CV (Fig. 34) data show that there are no surface oxidation or reduction peaks and that the Sb(111) | $EMImBF_4$ interface is nearly ideally polarisable

within the Sb(111) single crystal electrode potential region from −0.90 V to 0.10 V *vs.* Ag | AgCl | $EMImBF_4$.

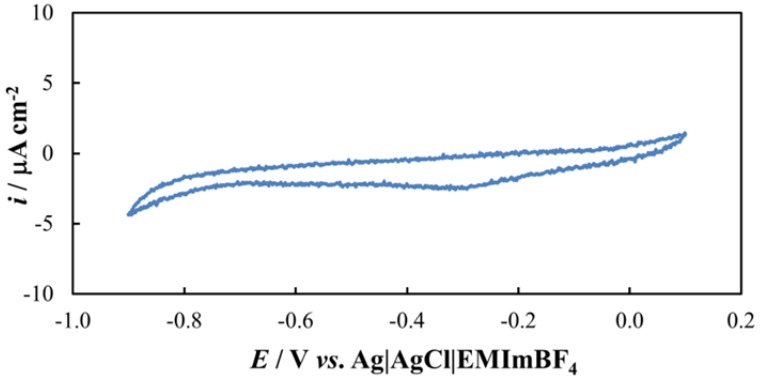

Figure 34. Current density (*i*) *vs.* electrode potential (*E*) curve for Sb(111) in $EMImBF_4$ at potential scan rate 10 mVs^{-1}.

The C_S *vs.* *E* curve (Fig. 35), measured at fixed frequency $f = 210$ Hz, shows the same kind of behaviour as for Bi(111) electrode in $EMImBF_4$ [164] and also for other non-aqueous electrolyte solutions at Bi(*hkl*) [165,166]. The C_S *vs.* *E* curve has a capacitance minimum around $E = -0.70$ V and a capacitance plateau (or maximum) at $E > -0.20$ V. The increase of capacitance values at more positive electrode potentials can be explained by the effect of the Sb surface electronic structure.

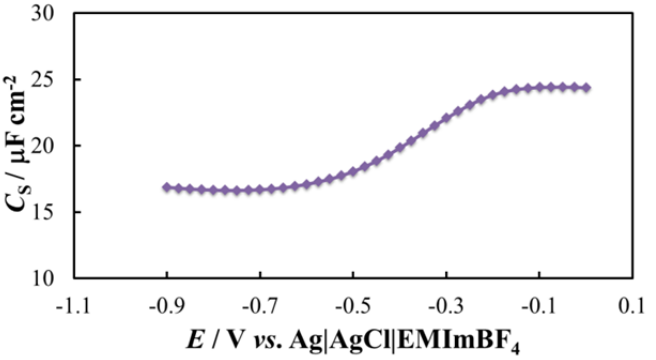

Figure 35. Series capacitance (C_S) *vs.* electrode potential (*E*) dependence for Sb(111) in $EMImBF_4$ at 210 Hz.

6.5. Surface structure of Sb(111) | $EMImBF_4$ + 2,2′-bipyridine solution interface

6.5.1. Analysis of CV and EIS data

CVs (Fig. 36) were measured within a potential region from −0.90 V to 0.10 V for Sb(111) | $EMImBF_4$ interface (orange curve, corresponding to the region of ideal polarisability) and from −1.00 V to 0.00 V for Sb(111) | $EMImBF_4$ + 1% 2,2′-BP (*vs*. Ag | AgCl | $EMImBF_4$) interface. Based on the data in Fig. 36, there are no surface oxidation or reduction peaks in the CVs at Sb(111) | $EMImBF_4$ interface.

The values of current density are somewhat higher for the $EMImBF_4$ + 1% 2,2′-BP solution at $E > -0.50$ V due to electrical double layer restructuring (charging and discharging) effects caused by the adsorption/desorption of 2,2′-BP molecules at Sb(111). The cathodic reduction process at $E < -0.90$ V for the Sb(111) | $EMImBF_4$ + 1% 2,2′-BP system likely corresponds to the formation of 2,2′-bipyridinium anions *via* the reductive desorption of 2,2′-BP molecules [45,167]. A quasi-reversible oxidation process is detected at the anodic extreme of the Sb(111) | $EMImBF_4$ + 1% 2,2′-BP system. This process takes place at moderate negative potentials, in comparison with the pure $EMImBF_4$ system, and thus, cannot be considered as the anodic dissolution of Sb. There is a very small reduction peak at $E = -0.10$ V (cathodic scan direction), which is independent of potential scanning rate, thus, indicating the adsorption/desorption step rate controlled process at the Sb(111) surface.

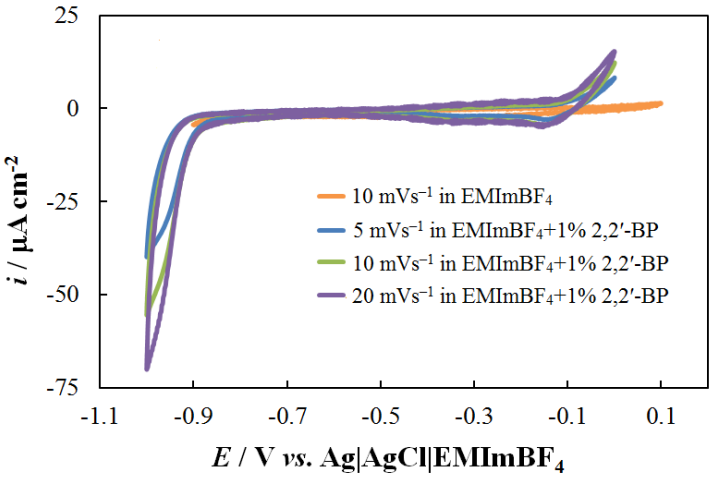

Figure 36. Current density (*i*) *vs*. electrode potential (*E*) curves for Sb(111) in $EMImBF_4$ and in $EMImBF_4$ + 1% 2,2′-BP at various potential scan rates (noted in figure).

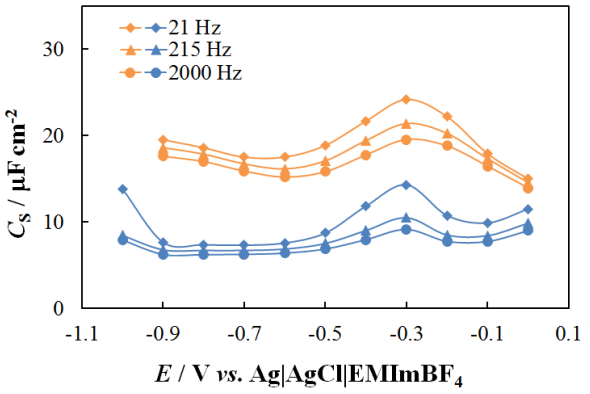

Figure 37. Series capacitance (C_S) *vs.* electrode potential (E) dependencies calculated from Nyquist plots at several fixed ac frequencies (noted in figure) for Sb(111) in $EMImBF_4$ (orange curves) and in $EMImBF_4$+1% 2,2′-BP (blue curves).

C_S *vs.* E curves show similar behaviour as in aqueous solutions [42] as the measured capacitance values decrease with an addition of 2,2′-BP in $EMImBF_4$ (Fig. 37). This indicates the formation of the compact adsorption layer at Sb(111) | $EMImBF_4$ + 2,2′-BP interface. The adsorption-desorption peak appears at the same electrode potentials ($E > -0.30$ V) where current density starts to increase in CVs. This confirms that the process is indeed caused by an adsorption process with partial charge transfer step that should be visualisable by *in situ* STM measurements. The C_S *vs.* E curve in Fig. 37 shows that the double layer capacitance of the 2,2′-BP system is consistently lower than that of the pure ionic liquid system (approximately 2.1 times lower near the C_S *vs.* E curve minimum) and, thus, similarly to organic compound adsorption, series capacitance decreases weakly with the increase of frequency.

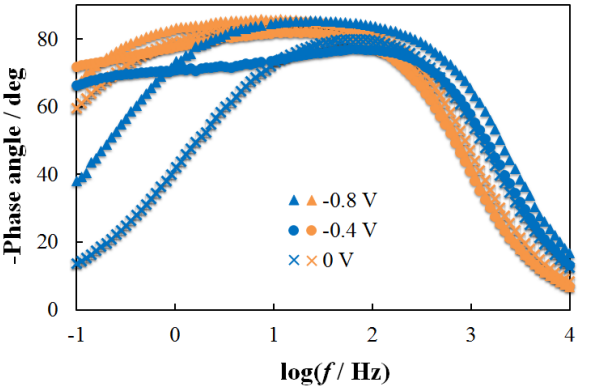

Figure 38. Phase angle *vs.* log f dependencies for Sb(111) in $EMImBF_4$ (orange marks) and in $EMImBF_4$ + 1% 2,2′-BP (blue marks) at several electrode potentials (*vs.* Ag | AgCl | $EMImBF_4$; noted in figure).

Analysis of the phase angle *vs*. log *f* curves (Fig. 38) shows that within the high frequency region, $f > 100$ Hz, the electrical double layer formation is faster after adding 2,2′-BP into $EMImBF_4$. At potentials near the maximum capacitance depression, $E = -0.70$ V, the double layer formation process is approximately 2.3 times faster for the $EMImBF_4$ + 1% 2,2′-BP system compared to pure $EMImBF_4$. However, the phase angle values are lower than -85^o for Sb(111) | $EMImBF_4$ in a wide range of frequency, showing only some deviations from the ideal capacitive behaviour at very low frequency values and at extreme electrode potentials ($E = 0.00$ V or $E = -0.80$ V). The log $-Z''$ *vs*. log *f* plots are linear within the *f* region from 100 Hz to 0.3 Hz with the slope values nearly −0.96, indicating the adsorption step limited process at Sb(111) | $EMImBF_4$ + 1% 2,2′-BP interface. Thus, the adsorption of 2,2′-BP at Sb(111) is limited mainly by the adsorption step rate. Mixed kinetic processes with partial charge transfer step can be seen at $E = 0.00$ V ($f \leq 10$ Hz). It is observed that at low *f* the phase angle values are significantly higher for the $EMImBF_4$ + 1% 2,2′-BP system than for the pure ionic liquid. This low frequency mixed kinetic process is interpreted to stem from the same adsorption/desorption process with partial charge transfer (at $E = 0.00$ V) or reductive desorption of 2,2′-BP molecules at $E < -0.80$ V as it was established from the analysis of the CV data.

6.5.2. Analysis of *in situ* STM data

Data in Fig. 39a show that at $E = -0.40$ V (*vs.* Ag | AgCl | $EMImBF_4$) 2,2′-BP molecules form a very tight pattern structure on the Sb(111) electrode surface if adsorbed from $EMImBF_4$+1% 2,2′-BP solution.

In the high-resolution *in situ* STM image for 2,2′-BP adsorption from $EMImBF_4$ + 1% 2,2′-BP solution (Fig. 39a), the periodic arrays of bright features are clearly visible at tip bias potential $E_{bias} = 50$ mV and at tunneling current 1.2 nA. From the FFT analysis (Fig. 39b) of the formed pattern surface electronic structure distances of 5.0 ± 0.2 Å and 8.5 ± 0.2 Å have been established. These experimental distances were used to construct a unit cell of the adlayer given in Fig. 39c. A stretched checkered pattern is seen to form with perpendicular unit cell distances of 5.0 Å and 8.6 Å, in a very good agreement with the experimental values. From the proposed unit cell parameters, the very high 2,2′-BP adlayer coverage 7.7×10^{-10} mol cm^{-2} has been calculated, which is much higher than that calculated for the Au(111) plane (3.8×10^{-10} to 4.4×10^{-10} mol cm^{-2}) [42].

After changing the potential to slightly less negative values ($E = -0.30$ V) and keeping it there for a few hours, a change in the adsorbed adlayer pattern has been established − the adlayer becomes even more tight, until the stretched checkered pattern transmutes into a striped pattern with distances 2.5 ± 0.2 Å, which prevails at even less negative potentials. The structure is probably based

on the π-π interaction of adsorbed 2,2′-BP molecules with the partial charge transfer between the Sb(111) surface and 2,2′-BP organic adlayer.

In order to get a better understanding of the bonding and interactions that determine the adsorption of 2,2′-BP from an ionic liquid the EIS and *in situ* STM results were complemented with modelling of the interfacial structure (Fig. 40).Three different positions at the Sb(111) surface (on atom, on bond, between 3 atoms) were considered as adsorption centres for modelling of the 2,2′-BP structure.

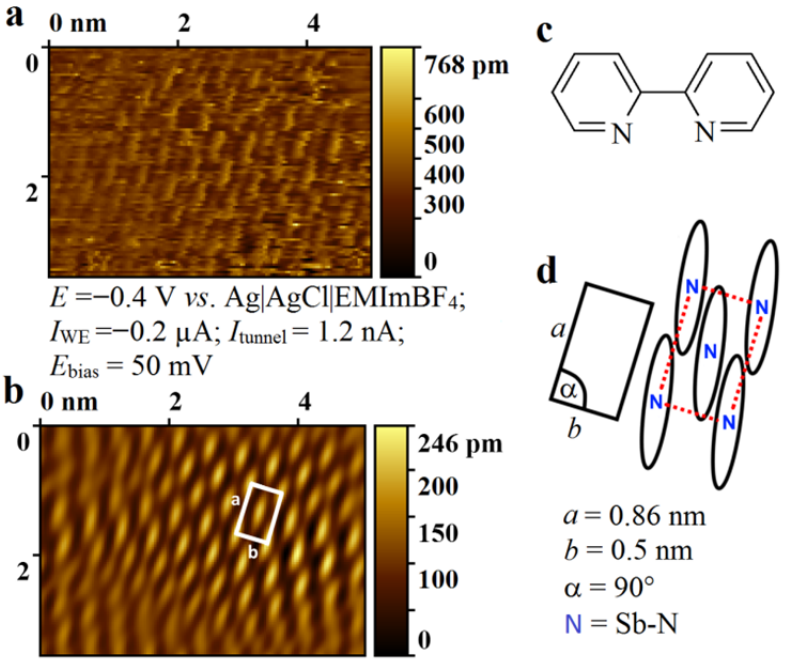

Figure 39. *In situ* STM image at electrode potential E = −0.4 V *vs.* Ag | AgCl | $EMImBF_4$ (a) and FFT filtered image (b) for 2,2′-BP adlayer at Sb(111), chemical structure of 2,2′-BP (c) and proposed packing model for 2,2′-BP molecules and calculated cell dimensions (d).

It has been detected that the 2,2′-BP molecules adsorb in the *cis*-orientation not only on single Sb atoms in the top position but also at the hollow positions between three Sb atoms to provide a higher degree of packaging. Hence, it was concluded that the adsorption of 2,2′-BP molecules is not highly directional and chemical bonding related, but rather connected to the formation of a closely packed interfacial 2D structure. It is also possible that one of the driving forces of 2,2′-BP adsorption on Sb(111) is the lack of strongly coordinating electron

pair acceptors in the $EMImBF_4$ medium. Overall, just a third of the 2,2′-BP molecules adsorb in the on top position on Sb(111) electrode surface while two thirds of the 2,2′-BP molecules adsorb in the hollow positions between three Sb atoms.

The substantial π-π stacking interaction between the adsorbed 2,2′-BP molecules stabilises the formed organic adlayer structure. Due to the directionality of the π-π stacking interaction, the adsorbed molecules form a striped pattern that has also been visualised by the *in situ* STM measurements.

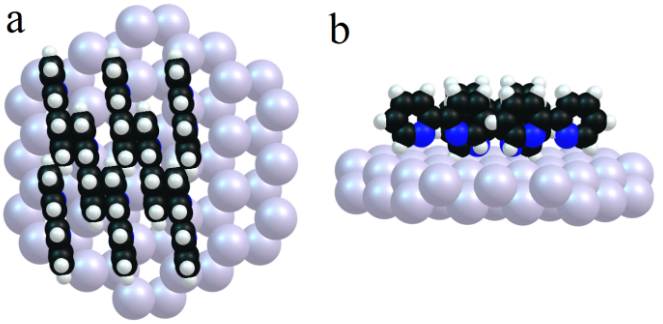

Figure 40. Models illustrating the possible orientation of adsorbed 2,2′-BP on the Sb(111) surface from above (a) and from the side (b).

7. SUMMARY

In this study *in situ* scanning tunneling microscopy (STM), cyclic voltammetry, electrochemical impedance spectroscopy and surface enhanced infrared absorption spectroscopy methods have been applied to study the interfacial structure of electrochemically polished Cd(0001) and Sb(111) single crystal electrodes in various electrolytes.

The studies revealed that the surface structure of Cd(0001) single crystal electrode is stable in the 0.1 M Na_2SO_4 + 1.0×10^{-5} M H_2SO_4 aqueous solution and in 1-ethyl-3-methylimidazolium tetrafluoroborate ($EMImBF_4$) under negative electrode potentials from −1.40 V to −0.90 V (*vs*. Ag | AgCl in sat. KCl aqueous solution) and from −1.60 V to −0.90 V (*vs*. Ag | AgCl | $EMImBF_4$), respectively. It was found that there are no quick surface reconstruction processes at Cd(0001) electrode surface. Similar behaviour was shown for Sb(111) in $EMImBF_4$ within electrode potential region from −1.10 V to −0.10 V (*vs*. Ag | AgCl | $EMImBF_4$).

The adsorption of 4,4′-bipyridine (4,4′-BP) from aqueous solution on Cd(0001) electrode and the adsorption of 2,2′-bipyridine (2,2′-BP) from $EMImBF_4$ ionic liquid on Sb(111) electrode has been analysed.

It was demonstrated by *in situ* STM data that at moderate negative electrode potential ($E = -1.25$ V *vs*. Ag | AgCl sat. KCl), the adsorbed 4,4′-BP molecules form parallel stripes on Cd(0001) surface with an adlayer coverage of 4.7×10^{-10} mol cm^{-2} and with fine structure parameters 2.70 nm between the stripes and 0.26 nm in the direction of the stripes.

2,2′-BP also forms a distinctive pattern when adsorbing at the Sb(111) surface from $EMImBF_4$. However this formed layer is significantly denser and the adlayer coverage is a very high 7.7×10^{-10} mol cm^{-2}.

Based on this study it can be concluded that the surface structure of Cd(0001) single crystal electrode is stable within wide electrode potential region in surface inactive aqueous electrolyte and the Cd(0001) electrode can be applied to study the adsorption of organic molecules from aqueous electrolytes.

The electrochemical stability of the Sb(111) | $EMImBF_4$ system has been demonstrated to be of excellent quality within wide potential region. Therefore, this system can be used to further study the adsorption of organic molecules from ionic liquids, as shown in the case of 2,2′-bipyridine in this study.

8. REFERENCES

[1] B. Koslowski, A. Tschetschetkin, N. Maurer, P. Ziemann, J. Kučera, A. Groß, J. Phys. Chem. C 117 (2013) 20060–20067.

[2] Q. Hang, F. Wang, P.D. Carpenter, D. Zemlyanov, D. Zakharov, E.A. Stach, W.E. Buhro, D.B. Janes, Nano Lett. 8 (2008) 49–55.

[3] J. Groll, M. Moeller, Methods Enzymol. 472 (2010) 1–18.

[4] H.P. Schreiber, M.R. Wertheimer, A.M. Wrobel, Thin Solid Films 72 (1980) 487–494.

[5] J.R. Santos Jr, L.H.C. Mattoso, A.J. Motheo, Electrochim. Acta 43 (1998) 309–313.

[6] D.G. Shchukin, M. Zheludkevich, K. Yasakau, S. Lamaka, M.G. Ferreira, H. Moehwald, Adv. Mater. 18 (2006) 1672–1678.

[7] R. Krishnan, M. Mackay, C. Hawker, B. Van Horn, Langmuir 21 (2005) 5770–5776.

[8] S.A. Burke, J.M. Topple, P. Grütter, J. Phys. Condens. Matter 21 (2009) 423101.

[9] A. Wang, A. Essner, V. Polineni, C. Stark, J. Dumbleton, Tribol. Int. 31 (1998) 17–33.

[10] V.V. Tsukruk, Adv. Mater. 13 (2001) 95–108.

[11] S.M. Hsu, Tribol. Int. 37 (2004) 553–559.

[12] A. Sayari, Chem. Mater. 8 (1996) 1840–1852.

[13] R. Noyori, T. Ohkuma, Angew. Chem. Int. Ed Engl. 40 (2001) 40–73.

[14] S.Y. Heriot, R.A.L. Jones, Nat. Mater. 4 (2005) 782–786.

[15] J.S. Wilkes, M.J. Zaworotko, Chem. Commun. 13 (1992) 965–967.

[16] H. Ohno, ed., Electrochemical Aspects of Ionic Liquids, Wiley & Sons, 2005.

[17] M. Galiński, A. Lewandowski, I. Stępniak, Electrochim. Acta 51 (2006) 5567–5580.

[18] M. Armand, F. Endres, D.R. MacFarlane, H. Ohno, B. Scrosati, Nat. Mater. 8 (2009) 621–629.

[19] H. Liu, Y. Liu, J. Li, Phys. Chem. Chem. Phys. 12 (2010) 1685–1697.

[20] R. Wiesendanger, H.-J. Güntherodt, Scanning Tunneling Microscopy II, Springer-Verlag, Berlin, 1992.

[21] M. Wilms, P. Broekmann, C. Stuhlmann, K. Wandelt, Surf. Sci. 416 (1998) 121–140.

[22] O.M. Magnussen, in:, P. Schmuki, S. Virtanen (Eds.), Electrochem. Nanoscale, Springer, New York, 2009, pp. 33–78.

[23] S. Kallip, H. Kasuk, V. Grozovski, P. Möller, E. Lust, Electrochim. Acta 53 (2008) 4035–4045.

[24] E. Lust, J. Erlich, U. Palm, Sov. Electrochem. 22 (1986) 659–662.

[25] T. Wandlowski, in:, A.J. Bard, M. Stratmann (Eds.), Encycl. Electrochem., Wiley VCH, Weinheim, 2002, pp. 383–471.

[26] D.M. Kolb, Prog. Surf. Sci. 51 (1996) 109–173.

[27] D. Mayer, T. Dretschkow, K. Ataka, T. Wandlowski, J. Electroanal. Chem. 524 (2002) 20–35.

[28] T. Dretschkow, T. Wandlowski, Electrochim. Acta 45 (1999) 731–740.

[29] H. Striegler, D. Krznarić, D.M. Kolb, J. Electroanal. Chem. 532 (2002) 227–235.

[30] E. Lust, A. Jänes, Russ. J. Electrochem. 30 (1994) 321–328.

[31] A. Jänes, E. Lust, Russ. J. Electrochem. 31 (1995) 596–599.

[32] E. Lust, A. Jänes, K. Lust, J. Erlich, Russ. J. Electrochem. 32 (1996) 552–564.

[33] A. Jänes, E. Lust, Russ. J. Electrochem. 32 (1996) 943–945.
[34] E. Lust, A. Jänes, K. Lust, R. Pullerits, J. Electroanal. Chem. 431 (1997) 183–201.
[35] E. Lust, A. Jänes, K. Lust, M. Väärtnõu, Electrochim. Acta 42 (1997) 771–783.
[36] E. Lust, A. Jänes, V. Sammelselg, P. Miidla, K. Lust, Electrochim. Acta 44 (1998) 373–383.
[37] S. Trasatti, E. Lust, in: White, R.E., Bockris, J.O'M., Conway, B.E. (Eds.), Mod. Asp. Electrochem., Kluwer Academic / Plenum Publishers, New York, 1999, pp. 1–193.
[38] E. Lust, A. Jänes, V. Sammelselg, P. Miidla, Electrochim. Acta 46 (2000) 185–191.
[39] S. Kallip, P. Laukkanen, A. Jänes, V. Sammelselg, J. Väyrynen, P. Miidla, E. Lust, Surf. Sci. 532–535 (2003) 1121–1126.
[40] V. Ivaništšev, A. Ruzanov, K. Lust, E. Lust, J. Electrochem. Soc. 160 (2013) H368–H375.
[41] T. Dretschkow, D. Lampner, T. Wandlowski, J. Electroanal. Chem. 458 (1998) 121–138.
[42] H. Noda, T. Minoha, L.-J. Wan, M. Osawa, J. Electroanal. Chem. 481 (2000) 62–68.
[43] F. Cunha, N.J. Tao, X.W. Wang, Q. Jin, B. Duong, J. D'Agnese, Langmuir 12 (1996) 6410–6418.
[44] T. Wandlowski, K. Ataka, D. Mayer, Langmuir 18 (2002) 4331–4341.
[45] V. Grozovski, V. Ivaništšev, H. Kasuk, T. Romann, E. Lust, Electrochim. Acta 120 (2014) 86–95.
[46] K.G. Baikerikar, S. Sathyanarayana, J. Electroanal. Chem. Interfacial Electrochem. 24 (1970) 333–344.
[47] V. Grozovski, S. Kallip, E. Lust, Surf. Sci. 613 (2013) 108–113.
[48] F.A. Cotton, G. Wilkinson, Advanced Inorganic Chemistry: A Comprehensive Text, 5th edition, John Wiley & Sons, New York, 1988.
[49] W.S. Khan, C. Cao, T. Mahmood, M. Ahmad, F.K. Butt, Z. Ali, Z. Usman, F. Wang, Qurrat ul Ain, Mater. Lett. 65 (2011) 1896–1899.
[50] H. Morrow, Kirk-Othmer Encycl. Chem. Technol. (2000) 1–36.
[51] B.P. Nikolskij, Spravochnik Himika. Tom 3. Himicheskoe Ravnovesie I Kinetika., Khimija, Moscow, 1964.
[52] A. Taylor, B.J. Kagle, Crystallographic Data on Metal and Alloy Structures, Dover, New York, 1963.
[53] D. Tromans, J. Electrochem. Soc. 156 (2009) C367–C376.
[54] E. Lust, K. Lust, A. Jänes, Russ. J. Electrochem. 31 (1995) 807–821.
[55] W.B. Pearson, The Crystal Chemistry and Physics of Metals and Alloys, Wiley-Interscience, New York, 1972.
[56] C.S. Barrett, P. Cucka, K. Haefner, Acta Crystallogr. 16 (1963) 451–453.
[57] D. Schiferl, Rev. Sci. Instrum. 48 (1977) 24–30.
[58] T.P. Moffat, in: A.J. Bard, M. Stratmann (Eds.), Encycl. Electrochem., Wiley-VCH, Weinheim, 2002, pp. 393–414.
[59] A. Hamelin, in: R.E. White, J.O. Bockris, B.E. Conway (Eds.), Mod. Asp. Electrochem., Plenum, New York, 1985, pp. 1–101.
[60] D.M. Kolb, Berichte Bunsenges. Für Phys. Chem. 92 (1988) 1175–1187.
[61] D.M. Kolb, in: J. Lipkowski, P.N. Ross (Eds.), Struct. Electrified Interfaces, VCH, New York, 1993, pp. 65–102.
[62] L.I. Daikhin, A.A. Kornyshev, M. Urbakh, J. Chem. Phys. 108 (1998) 1715–1723.

[63] H. Höchst, C.R. Ast, ICESS-9 Proc. 9th Int. Conf. Electron. Spectrosc. Struct. 137–140 (2004) 441–444.
[64] E. Lust, A. Jänes, Sov. Electrochem. 28 (1992) 650–653.
[65] F. Faridbod, M.R. Ganjali, P. Norouzi, S. Riahi, H. Rashedi, in: A. Kokorin (Ed.), Ion. Liq. Appl. Perspect., InTech, Croatia, 2011, pp. 643–657.
[66] F. Endres, S.Z. El Abedin, Phys. Chem. Chem. Phys. 8 (2006) 2101–2116.
[67] W. Liu, L. Cheng, Y. Zhang, H. Wang, M. Yu, J. Mol. Liq. 140 (2008) 68–74.
[68] K.N. Marsh, A. Deev, A.C.-T. Wu, E. Tran, A. Klamt, Korean J. Chem. Eng. 19 (2002) 357–362.
[69] T. Romann, O. Oll, P. Pikma, E. Lust, Electrochem. Commun. 23 (2012) 118–121.
[70] T. Romann, O. Oll, P. Pikma, H. Tamme, E. Lust, Electrochim. Acta 125 (2014) 183–190.
[71] K. Kubo, N. Hirai, T. Tanaka, S. Hara, Surf. Sci. 546 (2003) L785–L788.
[72] Y. Liu, Y.-X. Yuan, X.-R. Wang, N. Zhang, M.-M. Xu, J.-L. Yao, R.-A. Gu, J. Electroanal. Chem. 728 (2014) 10–17.
[73] G. Binning, H. Rohrer, C. Gerber, E. Weibel, Phys. Rev. Lett. 49 (1982) 57–61.
[74] J. Gomez, L. Vazquez, A.M. Baro, N. Garcia, C.L. Perdriel, W.E. Triaca, A.J. Arvia, Nature 323 (1986) 612–614.
[75] L. Vazquez, J.M. Rodríguez, J.G. Herrero, A.M. Baro, N. Garcia, J.C. Canullo, A.J. Arvia, Surf. Sci. 181 (1987) 98–106.
[76] L. Vazquez, A. Bartolome, A.M. Baro, C. Alonso, R.C. Salvarezza, A.J. Arvia, Surf. Sci. 215 (1989) 171–189.
[77] R. Sonnenfeld, P.K. Hansma, Science 232 (1986) 211–213.
[78] O. Lev, F.-R. Fan, A.J. Bard, J. Electrochem. Soc. 135 (1988) 783–784.
[79] P. Lustenberger, H. Rohrer, R. Christoph, H. Siegenthaler, J. Electroanal. Chem. Interfacial Electrochem. 243 (1988) 225–235.
[80] J. Wiechers, T. Twomey, D.M. Kolb, R.J. Behm, J. Electroanal. Chem. Interfacial Electrochem. 248 (1988) 451–460.
[81] V. Meunier, P. Lambin, in: Scanning Probe Microsc. Electr. Electromechanical Phenom. Nanoscale, Spreinger Science+Business Media, LLC, New York, 2007, pp. 455–479.
[82] S. Zhang, L. Li, A. Kumar, Materials Characterization Techniques, CRC Press, Taylor & Francis Group, Boco Raton, FL, 2009.
[83] D.M. Eigler, P.S. Weiss, E.K. Schweizer, N.D. Lang, Phys. Rev. Lett. 66 (1991) 1189–1192.
[84] W. Schmickler, J. Electroanal. Chem. Interfacial Electrochem. 296 (1990) 283–289.
[85] P. Sautet, Chem. Rev. 97 (1997) 1097–1116.
[86] P. Sautet, Surf. Sci. 374 (1997) 406–417.
[87] K.S. Birdi, Scanning Probe Microscopes : Applications in Science and Technology, CRC Press, Boca Raton, FL, 2003.
[88] V.L. Mironov, Fundamentals of Scanning Probe Microscopy, NT-MDT, Nizhniy Novgorod, 2004.
[89] M.A. Vorotyntsev, in: R.E. White, J.O. Bockris, B.E. Conway (Eds.), Mod. Asp. Electrochem., Plenum, New York, 1986, pp. 131–222.
[90] M.P. Soriaga, D.A. Harrington, J.L. Stikney, A. Wieckowski, in: R.E. White, J.O. Bockris, B.E. Conway (Eds.), Mod. Asp. Electrochem., Plenum, New York, 1996.

[91] D.M. Kolb, J. Schneider, Surf. Sci. 162 (1985) 764–775.
[92] X. Gao, G.J. Edens, A. Hamelin, M.J. Weaver, Surf. Sci. 296 (1993) 333–351.
[93] A. Hamelin, L. Stoicoviciu, J. Electroanal. Chem. Interfacial Electrochem. 271 (1989) 15–26.
[94] J. Clavilier, R. Faure, G. Guinet, R. Durand, J. Electroanal. Chem. Interfacial Electrochem. 107 (1979) 205–209.
[95] J. Clavilier, J. Electroanal. Chem. 107 (1980) 211–216.
[96] N. Batina, A.S. Dakkouri, D.M. Kolb, J. Electroanal. Chem. 370 (1994) 87–94.
[97] S. Kallip, E. Lust, Electrochem. Commun. 7 (2005) 863–867.
[98] V. Grozovski, H. Kasuk, S. Kallip, E. Lust, J. Electroanal. Chem. 712 (2014) 103–112.
[99] R. Jäger, S. Kallip, V. Grozovski, K. Lust, E. Lust, J. Electroanal. Chem. 622 (2008) 79–89.
[100] N.A. Hampson, R.J. Latham, J. Electroanal. Chem. 34 (1972) 247–249.
[101] W. Tikvic, B. Wielke, J. Cryst. Growth 34 (1976) 339–340.
[102] T. Thomberg, J. Electroanal. Chem. 485 (2000) 89–93.
[103] T. Thomberg, J. Nerut, E. Lust, Electrochim. Acta 49 (2004) 1271–1279.
[104] T. Thomberg, J. Nerut, E. Lust, J. Electroanal. Chem. 586 (2006) 237–246.
[105] M. Höpfner, W. Obretenov, K. Jüttner, W.J. Lorenz, G. Staikov, V. Bostanov, E. Budevski, Surf. Sci. 248 (1991) 225–233.
[106] W. Obretenov, M. Höpfner, W.J. Lorenz, E. Budevski, G. Staikov, H. Siegenthaler, Surf. Sci. 271 (1992) 191–200.
[107] J.W. Mathews, Epitaxial Growth, Academic Press, New York, 1975.
[108] G.L. Borges, M.G. Samant, K. Ashley, J. Electrochem. Soc. 139 (1992) 1565–1568.
[109] R. Gómez, M.J. Weaver, J. Electroanal. Chem. 435 (1997) 205–215.
[110] D.M. Kolb, J. Schneider, Electrochim. Acta 31 (1986) 929–936.
[111] P.A. Christensen, in: A.J. Bard, M. Stratmann, P.R. Unwin (Eds.), Encycl. Electrochem. Instrum. Electroanal. Chem., Wiley VCH, 2003, pp. 530–571.
[112] B.C. Smith, Fundamentals of Fourier Transform Infrared Spectroscopy, CRC Press, Boca Raton, 1996.
[113] T. Vo-Dinh, G. Gauglitz, Handbook of Spectroscopy, Wiley-VCH, Weinheim, 2003.
[114] A. Hartstein, J.R. Kirtley, J.C. Tsang, Phys. Rev. Lett. 45 (1980) 201–204.
[115] M. Osawa, Bull. Chem. Soc. Jpn. 70 (1997) 2861–2880.
[116] T. Romann, Preparation and Surface Modification of Bismuth Thin Film, Porous, and Microelectrodes, Thesis, 2010.
[117] T. Romann, O. Oll, P. Pikma, E. Lust, Electrochem. Commun. 23 (2012) 118–121.
[118] A.J. Bard, L.R. Faulkner, Electrochemical Methods: Fundamentals and Applications, 2nd ed., Wiley, New York, 2001.
[119] W. Schmickler, E. Santos, Interfacial Electrochemistry, 2nd ed., Springer, New York, 2010.
[121] B. Speiser, in: Encycl. Electrochem. Instrum. Electroanal. Chem., Wiley, New York, 2003, pp. 81–104.
[121] J.O. Bockris, A.K.N. Reddy, M. Gamboa-Aldeco, Modern Electrochemistry, 2nd ed., Kluwer Academic Publishers, New York, 2002.
[123] A. Lasia, in: Mod. Asp. Electrochem., Kluwer Academic / Plenum Publishers, New York, 1999, pp. 143–248.

[123] A.J. Bard, M. Stratmann, P.R. Unwin, eds., Encyclopedia of Electrochemistry: Instrumentation and Electroanalytical Chemistry v. 3, Wiley VCH, 2003.
[124] S. Uemura, R. Tanoue, N. Yilmaz, A. Ohira, M. Kunitake, Materials 3 (2010) 4252–4276.
[125] R. De Levie, Chem. Rev. 88 (1988) 599–609.
[126] C. Buess-Herman, Prog. Surf. Sci. 46 (1994) 335–375.
[127] Y.-X. Diao, M.-J. Han, L.-J. Wan, K. Itaya, T. Uchida, H. Miyake, A. Yamakata, M. Osawa, Langmuir 22 (2006) 3640–3646.
[129] M. Szklarczyk, J. Sobkowski, Electrochim. Acta 25 (1980) 1597–1601.
[129] O.M. Magnussen, Chem. Rev. 102 (2002) 679–726.
[130] E. Herrero, L.J. Buller, H.D. Abruna, Chem. Rev. 101 (2001) 1897–1930.
[131] K. Umemura, N. Nishida, M. Hara, H. Sasabe, W. Knoll, J. Electroanal. Chem. 438 (1997) 207–211.
[132] L.S. Pinheiro, M.L.A. Temperini, Appl. Surf. Sci. 171 (2001) 89–100.
[133] T. Dretschkow, T. Wandlowski, J. Electroanal. Chem. 467 (1999) 207–216.
[134] B. Xu, N.J. Tao, Science 301 (2003) 1221–1223.
[135] J. Pflaum, G. Bracco, F. Schreiber, R. Colorado Jr., O.E. Shmakova, T.R. Lee, G. Scoles, A. Kahn, Surf. Sci. 498 (2002) 89–104.
[136] T. Lu, T.M. Cotton, R.L. Birke, J.R. Lombardi, Langmuir 5 (1989) 406–414.
[138] K. Zawada, J. Bukowska, Electrochim. Acta 49 (2004) 469–476.
[138] V. Ivaništšev, R.R. Nazmutdinov, E. Lust, Surf. Sci. 604 (2010) 1919–1927.
[139] V. Ivaništšev, R.R. Nazmutdinov, E. Lust, Surf. Sci. 609 (2013) 91–99.
[140] L. Siinor, C. Siimenson, V. Ivaništšev, K. Lust, E. Lust, J. Electroanal. Chem. 668 (2012) 30–36.
[141] E. Anderson, V. Grozovski, L. Siinor, C. Siimenson, V. Ivaništšev, K. Lust, S. Kallip, E. Lust, J. Electroanal. Chem. 709 (2013) 46–56.
[142] I. Horcas, R. Fernández, J.M. Gómez-Rodríguez, J. Colchero, J. Gómez-Herrero, A.M. Baro, Rev. Sci. Instrum. 78 (2007) 013705.
[143] D. Nečas, P. Klapetek, Cent. Eur. J. Phys. 10 (2012) 181–188.
[144] T. Romann, E. Anderson, S. Kallip, H. Mändar, L. Matisen, E. Lust, Thin Solid Films 518 (2010) 3690–3693.
[145] B.B. Damaskin, O.A. Petrii, V.V. Batrakov, Adsorption of Organic Compounds on Electrodes, Plenum Press, New York, 1971.
[146] D. Rolle, J.W. Schultze, J. Electroanal. Chem. Interfacial Electrochem. 229 (1987) 141–164.
[147] A.R. Alumaa, U.V. Palm, Elektrokhimiya 6 (1970) 580–583.
[148] U.V. Palm, B.B. Damaskin, Itogi Nauki Tekhniki 12 (1977) 99–143.
[149] H. Kasuk, G. Nurk, K. Lust, E. Lust, J. Electroanal. Chem. 550 (2003) 13–31.
[150] V. Grozovski, H. Kasuk, S. Kallip, E. Lust, J. Electroanal. Chem. 712 (2014) 103–112.
[151] I.A. Vinokurov, M. Morin, J. Kankare, J. Phys. Chem. B 104 (2000) 5790–5796.
[153] S. Kallip, H. Kasuk, V. Grozovski, P. Möller, E. Lust, Electrochim. Acta 53 (2008) 4035–4045.
[153] R. Jäger, S. Kallip, V. Grozovski, K. Lust, E. Lust, J. Electroanal. Chem. 622 (2008) 79–89.
[154] G. Nurk, A. Jänes, K. Lust, E. Lust, J. Electroanal. Chem. 515 (2001) 17–32.
[156] V. Grozovski, V. Ivaništšev, H. Kasuk, T. Romann, E. Lust, Electrochim. Acta 120 (2014) 86–95.

[156] T.M. Cotton, M. Vavra, Chem. Phys. Lett. 106 (1984) 491–497.
[158] E. Lust, A. Jänes, V. Sammelselg, P. Miidla, K. Lust, Electrochim. Acta 44 (1998) 373–383.
[158] E. Lust, K. Lust, A. Jänes, Russ. J. Electrochem. 31 (1995) 807–821.
[159] E. Lust, A. Jänes, K. Lust, J. Erlich, Russ. J. Electrochem. 32 (1996) 552–564.
[160] D. Mayer, T. Dretschkow, K. Ataka, T. Wandlowski, J. Electroanal. Chem. 524 (2002) 20–35.
[161] L.G. Lin, Y. Wang, J.W. Yan, Y.Z. Yuan, J. Xiang, B.W. Mao, Electrochem. Commun. 5 (2003) 995–999.
[162] K. Tamura, S. Miyaguchi, K. Sakaue, Y. Nishihata, J. Mizuki, Electrochem. Commun. 13 (2011) 411–413.
[163] R. Atkin, N. Borisenko, M. Drüschler, F. Endres, R. Hayes, B. Huber, B. Roling, J. Mol. Liq. 192 (2014) 44–54.
[164] L. Siinor, K. Lust, E. Lust, J. Electrochem. Soc. 157 (2010) F83–F87.
[166] M. Väärtnõu, E. Lust, Electrochim. Acta 44 (1999) 2437–2444.
[167] M. Väärtnõu, E. Lust, Electrochim. Acta 47 (2001) 997–1005.
[167] M. Krejčik, A.A. Viček, J. Electroanal. Chem. Interfacial Electrochem. 313 (1991) 243–257.

9. SUMMARY IN ESTONIAN

Faasidevahelise piirpinna struktuur ja orgaaniliste ühendite adsorptisoon ioonsest vedelikust ja vesilahustest Cd(0001) ja Sb(111) elektroodidel: *in situ* STM uuringud

Tänapäeva teaduses ja tehnoloogias on olulisteks teemadeks moodsad energiasalvestusmeetodid ning nano- ja molekulaartehnoloogia. Tähelepanu keskmes on ioonsed vedelikud, mis leiavad rakendust paljudes energiasalvestus-seadmetes, näiteks superkondensaatorites, kuna nad on stabiilsed laias potentsiaalide vahemikus ja rakendatavad nii elektrolüüdi kui ka lahustina. Samuti leiavad väga laialdast rakendust pinnale rakendatava potentsiaali mõjul iseorganiseeruvad orgaaniliste ühendite monokihid, näiteks molekulaarmäludes ja korrosiooni inhibiitorites.

Selliste süsteemide loomiseks ja rakendamiseks tehnoloogias on vaja täpsemalt mõista elektroodi ja elektrolüüdi vahelisel piirpinnal toimuvate adsorptsiooniprotsesside olemust ja selle sõltuvust elektroodi potentsiaalist.

Käesolevas töös kasutati elektroodide pinnauuringute läbiviimiseks *in situ* skaneeriva tunnelmikroskoopia (STM) meetodit koos tsüklilise voltampero-meetria, impedantsspektroskoopia ja infrapunaspektroskoopia meetoditega. *In situ* STM meetodiga on võimalik reaalajas visualiseerida elektroodi atomaarne/ molekulaarne struktuur ja ka pinnale adsorbeeruvate ühendite paiknemise seaduspärasusi. Lisaks on võimalik uurida faasidevahelise piirpinna struktuuri sõltuvust rakendatavast potentsiaalist.

Antud töö eesmärkideks oli uurida elektrokeemilistelt poleeritud Cd(0001) ja Sb(111) monokristalsete elektroodide pinnale moodustunud struktuure erinevates elektrolüütides.

Töö käigus näidati, et monokristalse Cd(0001) elektroodi pinnastruktuur ei sõltu 0,1 M Na_2SO_4 + $1{,}0\times10^{-5}$ M H_2SO_4 vesilahuses ega ka 1-etüül-3-metüülimidasoolium tetrafluoroboraadis ($EMImBF_4$) pinnale rakendatavast potentsiaalist vahemikus vastavalt −1,40 V kuni −0,90 V (*vs* Ag | AgCl küllastunud KCl) ning −1,60 V kuni −0,90 V (*vs* Ag | AgCl | $EMImBF_4$). Tehti kindlaks, et neil piirpindadel ei toimu pindkihi reorganiseerumise protsesse. Samuti on Sb(111) elektroodi pinnastruktuur püsiv $EMImBF_4$-s potentsiaalide vahemikus −1,10 V kuni −0,10 V *vs* Ag | AgCl | $EMImBF_4$.

Uuriti 4,4′-bipüridiini (4,4′-BP) adsorptsiooni Cd(0001) elektroodile fooni lahusest ning 2,2′-bipüridiini (2,2′-BP) adsorptsiooni Sb(111) elektroodile ioonest vedelikust. Selgus, et 4,4′-BP molekulid moodustavad Cd(0001) elektroodile potentsiaalil −1,25 V (*vs* Ag | AgCl küllastunud KCl) paralleelsed molekulread pinnakatvusega $4{,}7\times10^{-10}$ mol cm^{-2}, kus molekuliridade vahelised kaugused on 2,70 nm ja molekulide vahelised kaugused ridades on 0,26 nm. Ka 2,2′-BP molekulid adsorbeeruvad Sb(111) pinnale $EMImBF_4$ ioonsest vedelikust korrapärase mustriga, kuid seda tunduvalt tihedama struktuuriga ning pinnakatvus on väga kõrge: $7{,}7\times10^{-10}$ mol cm^{-2}.

Läbiviidud uuringute põhjal võib öelda, et Cd(0001) monokristalse elektroodi pinnastruktuur pindinaktiivses elektrolüüdis (nii vesilahuses kui ka $EMImBF_4$ ioonses vedelikus) on püsiv kogu uuritud potentsiaalide vahemikus ning pinna rekonstrueerumise protsessi ei toimu. Seega on Cd(0001) elektroodi võimalik ka tulevikus rakendada uurimaks orgaaniliste ühendite adsorptsiooni vesilahustest.

Sb(111) | $EMImBF_4$ ioonne vedelik süsteem on väga stabiilsete elektrokeemiliste omadustega ning seda süsteemi võib ka tulevikus kasutada orgaaniliste ühendite monokihtide adsorptsiooni uurimiseks $EMImBF_4$ ioonsest vedelikust.

10. ACKNOWLEDGEMENTS

First of all I would like to express my greatest gratitude to my supervisor Professor Enn Lust for scientific guidance and support during the time of my studies.

Additionally I would like to thank Ph.D. Vitali Grozovski for all his advice on electrochemical polishing and *in situ* STM experiments, Ph.D. Liis Siinor and Ph.D. Heili Kasuk for introducing impedance spectroscopy method and helping with the analysis of data, M.Sc. Ove Oll and Ph.D. Tavo Romann for consultations and great help with infrared experiments and modelling, Rait Kanarbik and Ph.D. Margus Marandi for help with all my technical problems, Ph.D. Vladislav Ivaništšev for help with quantum chemical calculations, and Ph.D. Karmen Lust for her encouragement and useful critiques on my scientific writing.

I am very grateful to my family, especially my parents, for their support during my studies. I am thankful to my daughters for their love and laughter that kept me inspired and motivated.

Most of all I would like to thank my husband, Priit, who made it possible for me to spend long hours at Chemicum, whilst he stayed at home and took care of our beautiful daughters.

The present study was performed at the Institute of Chemistry of the University of Tartu and was financially supported by Estonian Energy Technology Program Project SLOKT10209T, Tartu University Institutional Research Project IUT20-13, Estonian Centres of Excellence in Science Project: High-technology Materials for Sustainable Development TK117, Estonian Research Foundation project ETF8786 and by graduate school „Functional materials and technologies“, receiving funding from the European Social Fund under project 1.2.0401.09-0079 in Estonia.

CURRICULUM VITAE

Name:	Piret Pikma
Date of birth:	November 30, 1985
Citizenship:	Estonian
Marital status:	Married, 2 children
Contact:	Institute of Chemistry, University of Tartu Ravila 14A, 50411, Tartu, Estonia
E-mail:	piret.pikma@ut.ee

Education:

2011–…	University of Tartu, Institute of Chemistry – *Ph.D.* student
2009–2011	University of Tartu, Institute of Chemistry – *M.Sc.* in physical and electrochemistry
2005–2009	University of Tartu, Institute of Chemistry – *B.Sc.* in chemistry

Professional Employment:

2011–…	University of Tartu, Institute of Chemistry, Chemist

List of publications:

T. Romann, O. Oll, **P. Pikma**, E. Lust, Abnormal infrared effects on bismuth thin film–$EMImBF_4$ ionic liquid interface, Electrochemistry Communications, 23, 118-121 (2012).

T. Romann, O. Oll, **P. Pikma**, H. Tamme, E. Lust, Surface chemistry of carbon electrodes in 1-ethyl-3-methylimidazolium tetrafluoroborate ionic liquid – an *in situ* infrared study, Electrochimica Acta, 125, 183-190 **(2014)**.

P. Pikma, V. Grozovski, H. Kasuk, E. Lust, *In situ* STM studies of electrochemically polished Cd(0001) electrode in aqueous electrolyte solutions, Surface Science, 628, 86-91 (2014).

T. Romann, O. Oll, **P. Pikma**, K. Kirsimäe, E. Lust, 4–10 V capacitors with graphene-based electrodes and ionic liquid electrolyte, Journal of Power Sources, 280, 606-611 (2015).

P. Pikma, L. Siinor, S. Selberg, E. Lust, *In situ* STM studies of electrochemically polished Cd(0001) electrode in 1-ethyl-3-methylimidazolium tetrafluoroborate, ECS Transactions, 66 (27), 41-47 (2015).

P. Pikma, H. Kasuk, O. Oll, V. Ivaništšev, T. Romann, V. Grozovski, K. Lust, E. Lust, Adsorption of 4,4′-bipyridine on the Cd(0001) single crystal electrode surface, Electrochimica Acta, 180, 965−976 (2015).

P. Pikma, L. Siinor, O. Oll, E. Lust, Formation of 2,2′-bipyridine adlayers at Sb(111) | ionic liquid + 2,2′-bipyridine solution interface, Electrochemistry Communications, *accepted* (2015).

ELULOOKIRJELDUS

Nimi:	Piret Pikma
Sünniaeg:	30. november 1985
Kodakondsus:	eestlane
Perekonnaseis:	Abielus, 2 last
Kontakt:	Keemia Instituut, Tartu Ülikool Ravila 14A, 50411, Tartu, Eesti
E-post:	piret.pikma@ut.ee

Haridus:

2011–…	Tartu Ülikool, Keemia Instituut – doktorant
2009–2011	Tartu Ülikool, Keemia Instituut – magistrikraad füüsikalise ja elektrokeemia erialal
2005–2009	Tartu Ülikool, Keemia Instituut – bakalaureusekraad keemia erialal

Teenistuskäik:

2011–…	Tartu Ülikool, Keemia Instituut, keemik

Teaduspublikatsioonid:

T. Romann, O. Oll, **P. Pikma**, E. Lust, Abnormal infrared effects on bismuth thin film–$EMImBF_4$ ionic liquid interface, Electrochemistry Communications, 23, 118-121 (2012).

T. Romann, O. Oll, **P. Pikma**, H. Tamme, E. Lust, Surface chemistry of carbon electrodes in 1-ethyl-3-methylimidazolium tetrafluoroborate ionic liquid – an *in situ* infrared study, Electrochimica Acta, 125, 183-190 (2014).

P. Pikma, V. Grozovski, H. Kasuk, E. Lust, *In situ* STM studies of electrochemically polished Cd(0001) electrode in aqueous electrolyte solutions, Surface Science, 628, 86-91 (2014).

T. Romann, O. Oll, **P. Pikma**, K. Kirsimäe, E. Lust, 4–10 V capacitors with graphene-based electrodes and ionic liquid electrolyte, Journal of Power Sources, 280, 606-611 (2015).

P. Pikma, L. Siinor, S. Selberg, E. Lust, *In situ* STM studies of electrochemically polished Cd(0001) electrode in 1-ethyl-3-methylimidazolium tetrafluoroborate, ECS Transactions, 66 (27), 41–47 (2015).

P. Pikma, H. Kasuk, O. Oll, V. Ivaništšev, T. Romann, V. Grozovski, K. Lust, E. Lust, Adsorption of 4,4′-bipyridine on the Cd(0001) single crystal electrode surface, Electrochimica Acta, 180, 965−976 (2015).

P. Pikma, L. Siinor, O. Oll, E. Lust, Formation of 2,2′-bipyridine adlayers at Sb(111) | ionic liquid + 2,2′-bipyridine solution interface, Electrochemistry Communications, *avaldamiseks vastu võetud* (2015).

DISSERTATIONES CHIMICAE UNIVERSITATIS TARTUENSIS

1. **Toomas Tamm.** Quantum-chemical simulation of solvent effects. Tartu, 1993, 110 p.
2. **Peeter Burk.** Theoretical study of gas-phase acid-base equilibria. Tartu, 1994, 96 p.
3. **Victor Lobanov.** Quantitative structure-property relationships in large descriptor spaces. Tartu, 1995, 135 p.
4. **Vahur Mäemets.** The ^{17}O and ^{1}H nuclear magnetic resonance study of H_2O in individual solvents and its charged clusters in aqueous solutions of electrolytes. Tartu, 1997, 140 p.
5. **Andrus Metsala.** Microcanonical rate constant in nonequilibrium distribution of vibrational energy and in restricted intramolecular vibrational energy redistribution on the basis of slater's theory of unimolecular reactions. Tartu, 1997, 150 p.
6. **Uko Maran.** Quantum-mechanical study of potential energy surfaces in different environments. Tartu, 1997, 137 p.
7. **Alar Jänes.** Adsorption of organic compounds on antimony, bismuth and cadmium electrodes. Tartu, 1998, 219 p.
8. **Kaido Tammeveski.** Oxygen electroreduction on thin platinum films and the electrochemical detection of superoxide anion. Tartu, 1998, 139 p.
9. **Ivo Leito.** Studies of Brønsted acid-base equilibria in water and non-aqueous media. Tartu, 1998, 101 p.
10. **Jaan Leis.** Conformational dynamics and equilibria in amides. Tartu, 1998, 131 p.
11. **Toonika Rinken.** The modelling of amperometric biosensors based on oxidoreductases. Tartu, 2000, 108 p.
12. **Dmitri Panov.** Partially solvated Grignard reagents. Tartu, 2000, 64 p.
13. **Kaja Orupõld.** Treatment and analysis of phenolic wastewater with microorganisms. Tartu, 2000, 123 p.
14. **Jüri Ivask.** Ion Chromatographic determination of major anions and cations in polar ice core. Tartu, 2000, 85 p.
15. **Lauri Vares.** Stereoselective Synthesis of Tetrahydrofuran and Tetrahydropyran Derivatives by Use of Asymmetric Horner-Wadsworth-Emmons and Ring Closure Reactions. Tartu, 2000, 184 p.
16. **Martin Lepiku.** Kinetic aspects of dopamine D_2 receptor interactions with specific ligands. Tartu, 2000, 81 p.
17. **Katrin Sak.** Some aspects of ligand specificity of P2Y receptors. Tartu, 2000, 106 p.
18. **Vello Pällin.** The role of solvation in the formation of iotsitch complexes. Tartu, 2001, 95 p.
19. **Katrin Kollist.** Interactions between polycyclic aromatic compounds and humic substances. Tartu, 2001, 93 p.

20. **Ivar Koppel.** Quantum chemical study of acidity of strong and superstrong Brønsted acids. Tartu, 2001, 104 p.
21. **Viljar Pihl.** The study of the substituent and solvent effects on the acidity of OH and CH acids. Tartu, 2001, 132 p.
22. **Natalia Palm.** Specification of the minimum, sufficient and significant set of descriptors for general description of solvent effects. Tartu, 2001, 134 p.
23. **Sulev Sild.** QSPR/QSAR approaches for complex molecular systems. Tartu, 2001, 134 p.
24. **Ruslan Petrukhin.** Industrial applications of the quantitative structure-property relationships. Tartu, 2001, 162 p.
25. **Boris V. Rogovoy.** Synthesis of (benzotriazolyl)carboximidamides and their application in relations with *N*- and *S*-nucleophyles. Tartu, 2002, 84 p.
26. **Koit Herodes.** Solvent effects on UV-vis absorption spectra of some solvatochromic substances in binary solvent mixtures: the preferential solvation model. Tartu, 2002, 102 p.
27. **Anti Perkson.** Synthesis and characterisation of nanostructured carbon. Tartu, 2002, 152 p.
28. **Ivari Kaljurand.** Self-consistent acidity scales of neutral and cationic Brønsted acids in acetonitrile and tetrahydrofuran. Tartu, 2003, 108 p.
29. **Karmen Lust.** Adsorption of anions on bismuth single crystal electrodes. Tartu, 2003, 128 p.
30. **Mare Piirsalu.** Substituent, temperature and solvent effects on the alkaline hydrolysis of substituted phenyl and alkyl esters of benzoic acid. Tartu, 2003, 156 p.
31. **Meeri Sassian.** Reactions of partially solvated Grignard reagents. Tartu, 2003, 78 p.
32. **Tarmo Tamm.** Quantum chemical modelling of polypyrrole. Tartu, 2003. 100 p.
33. **Erik Teinemaa.** The environmental fate of the particulate matter and organic pollutants from an oil shale power plant. Tartu, 2003. 102 p.
34. **Jaana Tammiku-Taul.** Quantum chemical study of the properties of Grignard reagents. Tartu, 2003. 120 p.
35. **Andre Lomaka.** Biomedical applications of predictive computational chemistry. Tartu, 2003. 132 p.
36. **Kostyantyn Kirichenko.** Benzotriazole – Mediated Carbon–Carbon Bond Formation. Tartu, 2003. 132 p.
37. **Gunnar Nurk.** Adsorption kinetics of some organic compounds on bismuth single crystal electrodes. Tartu, 2003, 170 p.
38. **Mati Arulepp.** Electrochemical characteristics of porous carbon materials and electrical double layer capacitors. Tartu, 2003, 196 p.
39. **Dan Cornel Fara.** QSPR modeling of complexation and distribution of organic compounds. Tartu, 2004, 126 p.
40. **Riina Mahlapuu.** Signalling of galanin and amyloid precursor protein through adenylate cyclase. Tartu, 2004, 124 p.

41. **Mihkel Kerikmäe.** Some luminescent materials for dosimetric applications and physical research. Tartu, 2004, 143 p.
42. **Jaanus Kruusma.** Determination of some important trace metal ions in human blood. Tartu, 2004, 115 p.
43. **Urmas Johanson.** Investigations of the electrochemical properties of polypyrrole modified electrodes. Tartu, 2004, 91 p.
44. **Kaido Sillar.** Computational study of the acid sites in zeolite ZSM-5. Tartu, 2004, 80 p.
45. **Aldo Oras.** Kinetic aspects of dATPαS interaction with $P2Y_1$ receptor. Tartu, 2004, 75 p.
46. **Erik Mölder.** Measurement of the oxygen mass transfer through the air-water interface. Tartu, 2005, 73 p.
47. **Thomas Thomberg.** The kinetics of electroreduction of peroxodisulfate anion on cadmium (0001) single crystal electrode. Tartu, 2005, 95 p.
48. **Olavi Loog.** Aspects of condensations of carbonyl compounds and their imine analogues. Tartu, 2005, 83 p.
49. **Siim Salmar.** Effect of ultrasound on ester hydrolysis in aqueous ethanol. Tartu, 2006, 73 p.
50. **Ain Uustare.** Modulation of signal transduction of heptahelical receptors by other receptors and G proteins. Tartu, 2006, 121 p.
51. **Sergei Yurchenko.** Determination of some carcinogenic contaminants in food. Tartu, 2006, 143 p.
52. **Kaido Tämm.** QSPR modeling of some properties of organic compounds. Tartu, 2006, 67 p.
53. **Olga Tšubrik.** New methods in the synthesis of multisubstituted hydrazines. Tartu. 2006, 183 p.
54. **Lilli Sooväli.** Spectrophotometric measurements and their uncertainty in chemical analysis and dissociation constant measurements. Tartu, 2006, 125 p.
55. **Eve Koort.** Uncertainty estimation of potentiometrically measured ph and pK_a values. Tartu, 2006, 139 p.
56. **Sergei Kopanchuk.** Regulation of ligand binding to melanocortin receptor subtypes. Tartu, 2006, 119 p.
57. **Silvar Kallip.** Surface structure of some bismuth and antimony single crystal electrodes. Tartu, 2006, 107 p.
58. **Kristjan Saal.** Surface silanization and its application in biomolecule coupling. Tartu, 2006, 77 p.
59. **Tanel Tätte.** High viscosity $Sn(OBu)_4$ oligomeric concentrates and their applications in technology. Tartu, 2006, 91 p.
60. **Dimitar Atanasov Dobchev**. Robust QSAR methods for the prediction of properties from molecular structure. Tartu, 2006, 118 p.
61. **Hannes Hagu**. Impact of ultrasound on hydrophobic interactions in solutions. Tartu, 2007, 81 p.

62. **Rutha Jäger.** Electroreduction of peroxodisulfate anion on bismuth electrodes. Tartu, 2007, 142 p.
63. **Kaido Viht.** Immobilizable bisubstrate-analogue inhibitors of basophilic protein kinases: development and application in biosensors. Tartu, 2007, 88 p.
64. **Eva-Ingrid Rõõm.** Acid-base equilibria in nonpolar media. Tartu, 2007, 156 p.
65. **Sven Tamp.** DFT study of the cesium cation containing complexes relevant to the cesium cation binding by the humic acids. Tartu, 2007, 102 p.
66. **Jaak Nerut.** Electroreduction of hexacyanoferrate(III) anion on Cadmium (0001) single crystal electrode. Tartu, 2007, 180 p.
67. **Lauri Jalukse.** Measurement uncertainty estimation in amperometric dissolved oxygen concentration measurement. Tartu, 2007, 112 p.
68. **Aime Lust.** Charge state of dopants and ordered clusters formation in CaF_2:Mn and CaF_2:Eu luminophors. Tartu, 2007, 100 p.
69. **Iiris Kahn**. Quantitative Structure-Activity Relationships of environmentally relevant properties. Tartu, 2007, 98 p.
70. **Mari Reinik.** Nitrates, nitrites, N-nitrosamines and polycyclic aromatic hydrocarbons in food: analytical methods, occurrence and dietary intake. Tartu, 2007, 172 p.
71. **Heili Kasuk.** Thermodynamic parameters and adsorption kinetics of organic compounds forming the compact adsorption layer at Bi single crystal electrodes. Tartu, 2007, 212 p.
72. **Erki Enkvist.** Synthesis of adenosine-peptide conjugates for biological applications. Tartu, 2007, 114 p.
73. **Svetoslav Hristov Slavov**. Biomedical applications of the QSAR approach. Tartu, 2007, 146 p.
74. **Eneli Härk.** Electroreduction of complex cations on electrochemically polished Bi(*hkl*) single crystal electrodes. Tartu, 2008, 158 p.
75. **Priit Möller.** Electrochemical characteristics of some cathodes for medium temperature solid oxide fuel cells, synthesized by solid state reaction technique. Tartu, 2008, 90 p.
76. **Signe Viggor.** Impact of biochemical parameters of genetically different pseudomonads at the degradation of phenolic compounds. Tartu, 2008, 122 p.
77. **Ave Sarapuu.** Electrochemical reduction of oxygen on quinone-modified carbon electrodes and on thin films of platinum and gold. Tartu, 2008, 134 p.
78. **Agnes Kütt.** Studies of acid-base equilibria in non-aqueous media. Tartu, 2008, 198 p.
79. **Rouvim Kadis.** Evaluation of measurement uncertainty in analytical chemistry: related concepts and some points of misinterpretation. Tartu, 2008, 118 p.
80. **Valter Reedo.** Elaboration of IVB group metal oxide structures and their possible applications. Tartu, 2008, 98 p.

81. **Aleksei Kuznetsov.** Allosteric effects in reactions catalyzed by the cAMP-dependent protein kinase catalytic subunit. Tartu, 2009, 133 p.
82. **Aleksei Bredihhin.** Use of mono- and polyanions in the synthesis of multisubstituted hydrazine derivatives. Tartu, 2009, 105 p.
83. **Anu Ploom.** Quantitative structure-reactivity analysis in organosilicon chemistry. Tartu, 2009, 99 p.
84. **Argo Vonk.** Determination of adenosine A_{2A}- and dopamine D_1 receptor-specific modulation of adenylate cyclase activity in rat striatum. Tartu, 2009, 129 p.
85. **Indrek Kivi.** Synthesis and electrochemical characterization of porous cathode materials for intermediate temperature solid oxide fuel cells. Tartu, 2009, 177 p.
86. **Jaanus Eskusson.** Synthesis and characterisation of diamond-like carbon thin films prepared by pulsed laser deposition method. Tartu, 2009, 117 p.
87. **Marko Lätt.** Carbide derived microporous carbon and electrical double layer capacitors. Tartu, 2009, 107 p.
88. **Vladimir Stepanov.** Slow conformational changes in dopamine transporter interaction with its ligands. Tartu, 2009, 103 p.
89. **Aleksander Trummal.** Computational Study of Structural and Solvent Effects on Acidities of Some Brønsted Acids. Tartu, 2009, 103 p.
90. **Eerold Vellemäe.** Applications of mischmetal in organic synthesis. Tartu, 2009, 93 p.
91. **Sven Parkel.** Ligand binding to 5-HT_{1A} receptors and its regulation by Mg^{2+} and Mn^{2+}. Tartu, 2010, 99 p.
92. **Signe Vahur.** Expanding the possibilities of ATR-FT-IR spectroscopy in determination of inorganic pigments. Tartu, 2010, 184 p.
93. **Tavo Romann**. Preparation and surface modification of bismuth thin film, porous, and microelectrodes. Tartu, 2010, 155 p.
94. **Nadežda Aleksejeva.** Electrocatalytic reduction of oxygen on carbon nanotube-based nanocomposite materials. Tartu, 2010, 147 p.
95. **Marko Kullapere.** Electrochemical properties of glassy carbon, nickel and gold electrodes modified with aryl groups. Tartu, 2010, 233 p.
96. **Liis Siinor.** Adsorption kinetics of ions at Bi single crystal planes from aqueous electrolyte solutions and room-temperature ionic liquids. Tartu, 2010, 101 p.
97. **Angela Vaasa.** Development of fluorescence-based kinetic and binding assays for characterization of protein kinases and their inhibitors. Tartu 2010, 101 p.
98. **Indrek Tulp.** Multivariate analysis of chemical and biological properties. Tartu 2010, 105 p.
99. **Aare Selberg.** Evaluation of environmental quality in Northern Estonia by the analysis of leachate. Tartu 2010, 117 p.
100. **Darja Lavõgina.** Development of protein kinase inhibitors based on adenosine analogue-oligoarginine conjugates. Tartu 2010, 248 p.

101. **Laura Herm.** Biochemistry of dopamine D_2 receptors and its association with motivated behaviour. Tartu 2010, 156 p.
102. **Terje Raudsepp.** Influence of dopant anions on the electrochemical properties of polypyrrole films. Tartu 2010, 112 p.
103. **Margus Marandi.** Electroformation of Polypyrrole Films: *In-situ* AFM and STM Study. Tartu 2011, 116 p.
104. **Kairi Kivirand.** Diamine oxidase-based biosensors: construction and working principles. Tartu, 2011, 140 p.
105. **Anneli Kruve.** Matrix effects in liquid-chromatography electrospray mass-spectrometry. Tartu, 2011, 156 p.
106. **Gary Urb.** Assessment of environmental impact of oil shale fly ash from PF and CFB combustion. Tartu, 2011, 108 p.
107. **Nikita Oskolkov.** A novel strategy for peptide-mediated cellular delivery and induction of endosomal escape. Tartu, 2011, 106 p.
108. **Dana Martin.** The QSPR/QSAR approach for the prediction of properties of fullerene derivatives. Tartu, 2011, 98 p.
109. **Säde Viirlaid.** Novel glutathione analogues and their antioxidant activity. Tartu, 2011, 106 p.
110. **Ülis Sõukand.** Simultaneous adsorption of Cd^{2+}, Ni^{2+}, and Pb^{2+} on peat. Tartu, 2011, 124 p.
111. **Lauri Lipping.** The acidity of strong and superstrong Brønsted acids, an outreach for the "limits of growth": a quantum chemical study. Tartu, 2011, 124 p.
112. **Heisi Kurig.** Electrical double-layer capacitors based on ionic liquids as electrolytes. Tartu, 2011, 146 p.
113. **Marje Kasari.** Bisubstrate luminescent probes, optical sensors and affinity adsorbents for measurement of active protein kinases in biological samples. Tartu, 2012, 126 p.
114. **Kalev Takkis.** Virtual screening of chemical databases for bioactive molecules. Tartu, 2012, 122 p.
115. **Ksenija Kisseljova**. Synthesis of aza-β^3-amino acid containing peptides and kinetic study of their phosphorylation by protein kinase A. Tartu, 2012, 104 p.
116. **Riin Rebane.** Advanced method development strategy for derivatization LC/ESI/MS. Tartu, 2012, 184 p.
117. **Vladislav Ivaništšev.** Double layer structure and adsorption kinetics of ions at metal electrodes in room temperature ionic liquids. Tartu, 2012, 128 p.
118. **Irja Helm.** High accuracy gravimetric Winkler method for determination of dissolved oxygen. Tartu, 2012, 139 p.
119. **Karin Kipper.** Fluoroalcohols as Components of LC-ESI-MS Eluents: Usage and Applications. Tartu, 2012, 164 p.
120. **Arno Ratas.** Energy storage and transfer in dosimetric luminescent materials. Tartu, 2012, 163 p.

121. **Reet Reinart-Okugbeni**. Assay systems for characterisation of subtype-selective binding and functional activity of ligands on dopamine receptors. Tartu, 2012, 159 p.
122. **Lauri Sikk.** Computational study of the Sonogashira cross-coupling reaction. Tartu, 2012, 81 p.
123. **Karita Raudkivi.** Neurochemical studies on inter-individual differences in affect-related behaviour of the laboratory rat. Tartu, 2012, 161 p.
124. **Indrek Saar.** Design of GalR2 subtype specific ligands: their role in depression-like behavior and feeding regulation. Tartu, 2013, 126 p.
125. **Ann Laheäär.** Electrochemical characterization of alkali metal salt based non-aqueous electrolytes for supercapacitors. Tartu, 2013, 127 p.
126. **Kerli Tõnurist.** Influence of electrospun separator materials properties on electrochemical performance of electrical double-layer capacitors. Tartu, 2013, 147 p.
127. **Kaija Põhako-Esko.** Novel organic and inorganic ionogels: preparation and characterization. Tartu, 2013, 124 p.
128. **Ivar Kruusenberg.** Electroreduction of oxygen on carbon nanomaterial-based catalysts. Tartu, 2013, 191 p.
129. **Sander Piiskop.** Kinetic effects of ultrasound in aqueous acetonitrile solutions. Tartu, 2013, 95 p.
130. **Ilona Faustova**. Regulatory role of L-type pyruvate kinase N-terminal domain. Tartu, 2013, 109 p.
131. **Kadi Tamm.** Synthesis and characterization of the micro-mesoporous anode materials and testing of the medium temperature solid oxide fuel cell single cells. Tartu, 2013, 138 p.
132. **Iva Bozhidarova Stoyanova-Slavova.** Validation of QSAR/QSPR for regulatory purposes. Tartu, 2013, 109 p.
133. **Vitali Grozovski**. Adsorption of organic molecules at single crystal electrodes studied by *in situ* STM method. Tartu, 2014, 146 p.
134. **Santa Veikšina**. Development of assay systems for characterisation of ligand binding properties to melanocortin 4 receptors. Tartu, 2014, 151 p.
135. **Jüri Liiv.** PVDF (polyvinylidene difluoride) as material for active element of twisting-ball displays. Tartu, 2014, 111 p.
136. **Kersti Vaarmets.** Electrochemical and physical characterization of pristine and activated molybdenum carbide-derived carbon electrodes for the oxygen electroreduction reaction. Tartu, 2014, 131 p.
137. **Lauri Tõntson**. Regulation of G-protein subtypes by receptors, guanine nucleotides and Mn^{2+}. Tartu, 2014, 105 p.
138. **Aiko Adamson.** Properties of amine-boranes and phosphorus analogues in the gas phase. Tartu, 2014, 78 p.
139. **Elo Kibena**. Electrochemical grafting of glassy carbon, gold, highly oriented pyrolytic graphite and chemical vapour deposition-grown graphene electrodes by diazonium reduction method. Tartu, 2014, 184 p.

140. **Teemu Näykki.** Novel Tools for Water Quality Monitoring – From Field to Laboratory. Tartu, 2014, 202 p.
141. **Karl Kaupmees.** Acidity and basicity in non-aqueous media: importance of solvent properties and purity. Tartu, 2014, 128 p.
142. **Oleg Lebedev**. Hydrazine polyanions: different strategies in the synthesis of heterocycles. Tartu, 2015, 118 p.
143. **Geven Piir.** Environmental risk assessment of chemicals using QSAR methods. Tartu, 2015, 123 p.
144. **Olga Mazina.** Development and application of the biosensor assay for measurements of cyclic adenosine monophosphate in studies of G protein-coupled receptor signalinga. Tartu, 2015, 116 p.
145. **Sandip Ashokrao Kadam.** Anion receptors: synthesis and accurate binding measurements. Tartu, 2015, 116 p.
146. **Indrek Tallo.** Synthesis and characterization of new micro-mesoporous carbide derived carbon materials for high energy and power density electrical double layer capacitors. Tartu, 2015, 148 p.
147. **Heiki Erikson.** Electrochemical reduction of oxygen on nanostructured palladium and gold catalysts. Tartu, 2015, 204 p.
148. **Erik Anderson.** *In situ* Scanning Tunnelling Microscopy studies of the interfacial structure between Bi(111) electrode and a room temperature ionic liquid. Tartu, 2015, 118 p.
149. **Girinath G. Pillai.** Computational Modelling of Diverse Chemical, Biochemical and Biomedical Properties. Tartu, 2015, 140 p.